



LAWRENCE
LIVERMORE
NATIONAL
LABORATORY

Numerical Methods for Solid Mechanics on Overlapping Grids: Linear Elasticity

Daniel Appelo, Jeffrey W. Banks, William D. Henshaw, Donald W. Schwendeman

January 7, 2010

Journal of Computational Physics

Disclaimer

This document was prepared as an account of work sponsored by an agency of the United States government. Neither the United States government nor Lawrence Livermore National Security, LLC, nor any of their employees makes any warranty, expressed or implied, or assumes any legal liability or responsibility for the accuracy, completeness, or usefulness of any information, apparatus, product, or process disclosed, or represents that its use would not infringe privately owned rights. Reference herein to any specific commercial product, process, or service by trade name, trademark, manufacturer, or otherwise does not necessarily constitute or imply its endorsement, recommendation, or favoring by the United States government or Lawrence Livermore National Security, LLC. The views and opinions of authors expressed herein do not necessarily state or reflect those of the United States government or Lawrence Livermore National Security, LLC, and shall not be used for advertising or product endorsement purposes.

Numerical Methods for Solid Mechanics on Overlapping Grids: Linear Elasticity

Daniel Appelö¹

California Institute of Technology, Pasadena, CA 91125, appelo@caltech.edu

Jeffrey W. Banks, William D. Henshaw²

Centre for Applied Scientific Computing, Lawrence Livermore National Laboratory, Livermore, CA 94551, banks20@llnl.gov

Donald W. Schwendeman³

*Department of Mathematical Sciences, Rensselaer Polytechnic Institute, Troy, NY 12180,
schwed@rpi.edu*

Abstract

We describe and evaluate two numerical approaches for solving the equations of linear elasticity on composite overlapping grids. In the first approach we solve the elastodynamic equations posed as a second-order system (SOS) using a conservative finite difference approximation. In the second approach we solve the equations written as a first order system (FOS) using a high-order characteristic-based (Godunov) finite-volume method. We describe the approximations to the equations and boundary conditions for each scheme. We analyse the stability of the first-order and second-order scalar wave equations on an overlapping grid and show that non-dissipative approximations can have unstable modes with growth rates proportional to the inverse of the mesh spacing. We show that the addition of a high-order filter can be used to stabilize the SOS scheme while the upwinding nature of the Godunov scheme naturally stabilizes the FOS scheme. We discuss the use adaptive mesh refinement with both approaches. The accuracy of the two schemes is compared and verified using the method of analytic solutions and for problems with known solutions. A posteriori error estimates for a complex example of a three-dimensional plate with holes provides an additional verification of the second-order accuracy of the schemes. Performance results comparing the two schemes are also presented.

Contents

1	Introduction	2
2	Governing equations	3
3	Overlapping grid framework	4
4	Discretization of the governing equations	4
4.1	Second-order system	5
4.2	First-order system	7
5	Boundary Conditions	9
5.1	Boundary conditions for the second-order system	9

¹ caltech stuff

² This work was performed under the auspices of the U.S. Department of Energy (DOE) by Lawrence Livermore National Laboratory under Contract DE-AC52-07NA27344 and by DOE contracts from the ASCR Applied Math Program.

³ This research was supported by Lawrence Livermore National Laboratory under subcontract B548468, and by the National Science Foundation under grants DMS-0532160 and DMS-0609874.

5.2	Boundary conditions for the first-order system	10
6	Stability at overlapping grid interfaces with nearby boundaries	11
6.1	Stability of the second-order wave equation	11
6.2	Stability of the first-order wave equation	17
7	Adaptive Mesh Refinement	20
8	Numerical results	21
8.1	The method of analytic solutions	21
8.2	Circular void in a square	22
8.3	Spherical void in a box	23
8.4	Traveling pulse with AMR	25
8.5	Vibrational modes of an elastic annulus	27
8.6	Vibrational modes of an elastic sphere	29
8.7	Diffraction of a p-wave “shock” by a cylindrical cavity	32
8.8	Performance	32
8.9	Three-dimensional circular plate with holes	34
9	Conclusions	35
	References	36

1. Introduction

The simulation of the deformation of solids is an important and well established field. Approaches based on Galerkin approximations and the finite element method are widely used. Finite difference, finite volume and spectral element methods are also commonly used. In this work we consider the solution to solid mechanics problems using composite overlapping grids and adaptive mesh refinement (AMR). An overlapping grid consists of a collection of structured grids that cover a domain and overlap where they meet [1]. Solution values on different grids are matched by interpolation at the overlapping boundaries. Overlapping grids can be used to develop efficient methods through the use of structured grids and Cartesian grids. They can provide smooth, boundary-fitted grids for complex geometry which is important in providing accurate results for wave propagation problems. Overlapping grids have been used to solve a wide class of problems. They have primarily been used for fluid dynamics (see [2,3] and the references therein) but more recently have also been applied to electromagnetics [4]. Overlapping grids were utilized for modeling linear elastic waves in [5–7]. The current work, however, appears to be the first careful analysis of the accuracy and stability of using general curvilinear overlapping grids for elastodynamic problems.

We describe and compare two numerical approaches for solving the equations of linear elasticity on overlapping grids. In the first approach, denoted as SOS-C, we solve the equations posed as a second-order-system (SOS) for the displacement using a conservative finite difference approximation. On a single curvilinear grid the SOS-C scheme is stable, non-dissipative and energy preserving. In the second approach, denoted by FOS-G, we solve the equations written as a first-order-system (FOS) for the displacement, velocity and stress using a high-order finite-volume (Godunov) method. The two schemes are compared in terms of accuracy, stability and performance. The stability of the schemes on overlapping grids is also studied through the normal mode analysis of some model problems.

It is known that finite difference methods for the SOS may have difficulty at traction (stress free) boundaries when the ratio λ/μ of the Lamé parameters becomes large. Application of the traction boundary conditions, which involve normal and tangential derivatives of the displacement, must be done with care to avoid numerical instabilities. On a single grid, the SOS-C scheme uses an approximation at traction boundaries that is always stable. The basic SOS-C scheme is neutrally stable with no dissipation. This is an attractive property for wave propagation problems but also means that small changes to the numerical approximation could result in an unstable scheme. Indeed, the interpolation equations on overlapping grids will in general excite an instability in the SOS-C scheme. In addition, when narrow curvilinear grids are used near physical boundaries, an unstable mode generated from the interpolation equations may be amplified due to interactions with the nearby boundary. This instability is stronger than the one created from an isolated interpolation boundary as shown by computations and by our analysis (section 6). We show that the addition of a high-order low-pass filter can be used to stabilize the SOS-C scheme in both these cases. The FOS-G scheme, by comparison, does not have difficulty in treating traction boundaries, even as the ratio

of λ/μ becomes large. This is related to the fact that the first-order-system directly evolves the components of the stress and thus the traction boundary condition acts more as a Dirichlet boundary condition.

The adaptive mesh refinement (AMR) technique dynamically adds refinement grids as the solution evolves to regions where more resolution is required. This approach is particularly effective when there are small regions in the domain where greater resolution is required. We apply the AMR technique with the SOS-C and FOS-G schemes. Refinement grids are added in the parameter space of each base grid of the overlapping grid. Grids are regenerated every few time steps. An example of a compression wave diffracting around a cylindrical void is used to illustrate the use of AMR.

An outline of the paper now follows. In Section 2 we present the governing equations and boundary conditions. A brief description of the overlapping grid approach is provided in Section 3. The SOS-C and FOS-G numerical schemes are described in Section 4 and approximations to boundary conditions in Section 5. Aspects of the stability of our approximations on overlapping grids are considered in Section 6. The AMR approach is discussed in Section 7. Numerical results are presented in Section 8. A variety of tests are considered to verify the accuracy of the two approaches. The computational performance of the schemes are also compared. The final section gives concluding remarks.

2. Governing equations

Consider an elastic solid that at time $t = 0$ occupies the domain $\Omega \subset \mathbb{R}^{n_d}$ in $n_d = 2$ or $n_d = 3$ space dimensions. Let $\mathbf{u}(\mathbf{x}, t)$, with components $u_i(\mathbf{x}, t)$, denote the displacement of a material particle originally located at position $\mathbf{x} \in \mathbb{R}^{n_d}$ and let $\boldsymbol{\sigma}(\mathbf{x}, t)$ denote the Cauchy stress tensor with components $\sigma_{ij}(\mathbf{x}, t)$. It is assumed that the solid is a homogeneous isotropic material, and that the evolution of the displacement is governed by the equations of linear elasticity given by (with Einstein summation convention),

$$\rho_0 \frac{\partial^2 u_i}{\partial t^2} = \frac{\partial \sigma_{ij}}{\partial x_j} + \rho_0 f_i, \quad \mathbf{x} \in \Omega, \quad t > 0, \quad i = 1, 2, \dots, n_d, \quad (1)$$

where ρ_0 is the density of the material, \mathbf{f} is an acceleration due to an applied body force, and the components of σ_{ij} are given by

$$\sigma_{ij} = \lambda (\epsilon_{kk}) \delta_{ij} + 2\mu \epsilon_{ij}, \quad \epsilon_{ij} = \frac{1}{2} \left(\frac{\partial u_i}{\partial x_j} + \frac{\partial u_j}{\partial x_i} \right). \quad (2)$$

Here, ϵ_{ij} is the (linear) strain tensor, δ_{ij} is the identity tensor, $\epsilon_{kk} = \sum_k \epsilon_{kk} = \nabla \cdot \mathbf{u}$ is the divergence, and λ and μ are the Lamé parameters, related to Young's modulus E and Poisson's ratio ν by

$$\mu = \frac{E}{2(1+\nu)}, \quad \lambda = \frac{\nu E}{(1+\nu)(1-2\nu)}. \quad (3)$$

The initial conditions for the second-order-system (1) are

$$\mathbf{u}(\mathbf{x}, 0) = \mathbf{u}_0(\mathbf{x}), \quad \frac{\partial \mathbf{u}}{\partial t}(\mathbf{x}, 0) = \mathbf{v}_0(\mathbf{x}), \quad \mathbf{x} \in \Omega, \quad (4)$$

where $\mathbf{u}_0(\mathbf{x})$ and $\mathbf{v}_0(\mathbf{x})$ are the initial displacement and velocity of the solid, respectively. The boundary conditions for (1) are applied for $\mathbf{x} \in \partial\Omega$ and may take various forms. The boundary conditions considered in this paper are

$$\mathbf{u} = \mathbf{g}_d(\mathbf{x}, t), \quad \text{displacement boundary conditions,} \quad (5)$$

$$\mathbf{n} \cdot \boldsymbol{\sigma} = \mathbf{g}_t(\mathbf{x}, t), \quad \text{traction boundary conditions,} \quad (6)$$

$$\left. \begin{aligned} \mathbf{n} \cdot \mathbf{u} &= g_s(\mathbf{x}, t) \\ \mathbf{n} \cdot \boldsymbol{\sigma} \cdot \boldsymbol{\tau}_m &= g_{s,m}(\mathbf{x}, t) \end{aligned} \right\} \quad \text{slip-wall boundary conditions.} \quad (7)$$

Here, \mathbf{n} is the unit outward normal on the boundary, $\boldsymbol{\tau}_m$, $m = 1, \dots, n_d - 1$ are unit and orthogonal tangent vectors, $\mathbf{g}_d(\mathbf{x}, t)$, $\mathbf{g}_t(\mathbf{x}, t)$, are the given displacement and traction at the boundary, respectively, while $g_s(\mathbf{x}, t)$ and $g_{s,m}(\mathbf{x}, t)$ define the slip wall motion.

We also consider the equations in (1) and (2) written as a first-order system

$$\begin{aligned}\frac{\partial u_i}{\partial t} &= v_i, \\ \frac{\partial v_i}{\partial t} &= \frac{1}{\rho_0} \frac{\partial \sigma_{ij}}{\partial x_j} + f_i, \\ \frac{\partial \sigma_{ij}}{\partial t} &= \lambda (\dot{\epsilon}_{kk}) \delta_{ij} + 2\mu \dot{\epsilon}_{ij},\end{aligned}\tag{8}$$

where $\mathbf{v}(\mathbf{x}, t)$ is the velocity and the components of the rate of strain tensor $\dot{\epsilon}_{ij}$ are given by

$$\dot{\epsilon}_{ij} = \frac{1}{2} \left(\frac{\partial v_i}{\partial x_j} + \frac{\partial v_j}{\partial x_i} \right).$$

The initial conditions for $u_i(\mathbf{x}, 0)$, $v_i(\mathbf{x}, 0)$ and $\sigma_{ij}(\mathbf{x}, 0)$ for the FOS are derived from the initial conditions (4) for the SOS. The governing equations, whether written as a first or second-order system, are hyperbolic and represent the motion of elastic waves in the solid. For the SOS, the characteristic wave speeds are $\pm c_p$ and $\pm c_s$ where the pressure and shear wave speeds are given by

$$c_p = \sqrt{\frac{\lambda + 2\mu}{\rho_0}}, \quad c_s = \sqrt{\frac{\mu}{\rho_0}}.\tag{9}$$

The FOS has the additional wave speed of 0.

3. Overlapping grid framework

An overlapping grid, \mathcal{G} , consists of a set of structured component grids, $\{G_g\}$, $g = 1, \dots, \mathcal{N}$, that cover the domain Ω and overlap where the component grids meet. Typically, boundary-fitted curvilinear grids are used near the boundaries while one or more background Cartesian grids are used to handle the bulk of the domain. Each component grid is a logically rectangular, curvilinear grid in n_d space dimensions ($n_d = 2$ or 3), and is defined by a smooth mapping from parameter space \mathbf{r} (the unit square or cube) to physical space \mathbf{x} ,

$$\mathbf{x} = \mathbf{G}_g(\mathbf{r}), \quad \mathbf{r} \in [0, 1]^{n_d}, \quad \mathbf{x} \in \mathbb{R}^{n_d}.$$

This mapping is also used to define the location of grid points at any desired resolution as required when the grid is refined (see Section 7).

Figure 1 shows a simple overlapping grid consisting of two component grids, an annular boundary-fitted grid and a background Cartesian grid. The top view shows the overlapping grid while the bottom view shows each grid in parameter space. In this example the annular grid cuts a hole in the Cartesian grid so that the latter grid has a number of unused points which are marked as open circles. The other points on the component grids are marked as discretization points (where the PDE or boundary conditions are discretized) and interpolation points. Solution values at interpolation points are generally determined by a tensor-product Lagrange interpolant in the parameter space of the donor grid. Ghost points are used to facilitate the discretization of boundary conditions.

The classification of points on a grid into discretization, interpolation and unused points is determined by an overlapping grid generator. We use the Ogen grid generator [8]. Ogen takes as input a set of overlapping component grids along with a classification of the boundaries of each grid as a physical boundary, an interpolation boundary or a periodic boundary. Unused points are determined by Ogen using physical boundaries to mark points exterior to the domain following a *hole-cutting* algorithm. The remaining points are classified as either discretization points or interpolation points.

4. Discretization of the governing equations

The discretization of the governing equations is carried out on a uniform grid in the unit computational space $\mathbf{r} \in [0, 1]^{n_d}$. The mapping $\mathbf{x} = \mathbf{G}_g(\mathbf{r})$ defines the grid in physical space \mathbf{x} , and an exact changes

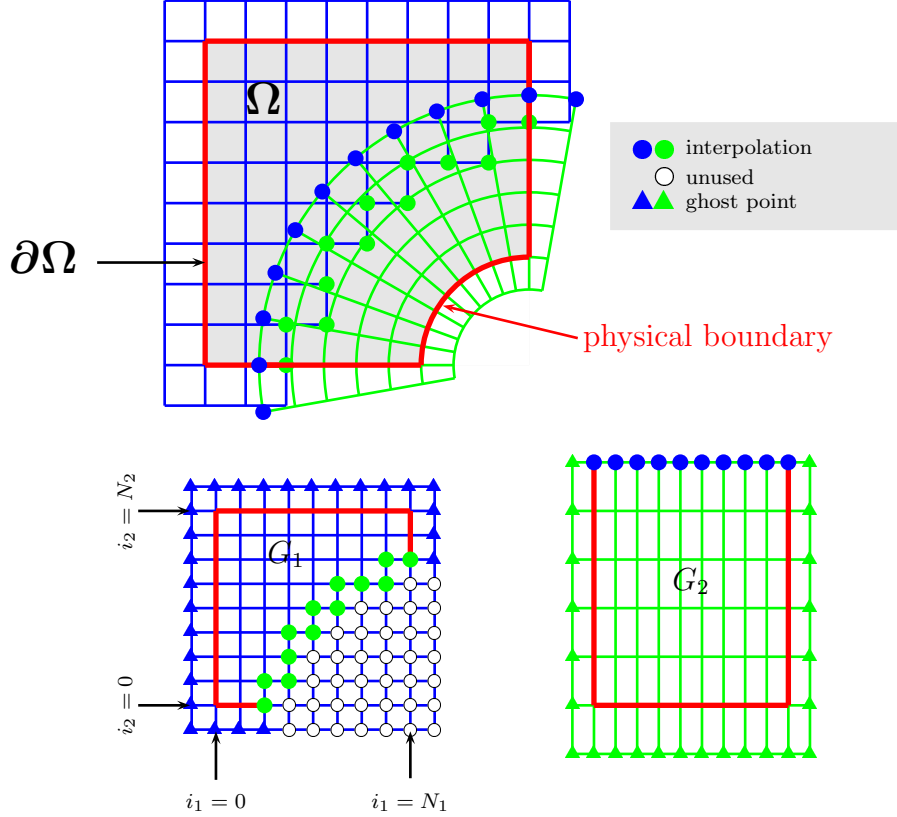


Fig. 1. The top view shows an overlapping grid consisting of two structured curvilinear component grids. The bottom views show the component grids in the unit square parameter space. Grid points are classified as discretization points, interpolation points or unused points. Ghost points are used to apply boundary conditions.

of variables is made to express the governing equations in computational space. A discretization is then performed on the mapped equations. This is described for the second and first-order systems in the two subsections below.

4.1. Second-order system

In this section we describe the discretization of the governing equations (1) posed as a second-order system. The equations (1)-(2) for the second-order-system are discretized in conservation form. Given the mapping, $\mathbf{x} = \mathbf{G}(\mathbf{r})$, defining the grid transformation, the equations can be written in conservation form

$$\begin{aligned}\rho_0 \frac{\partial^2 u_i}{\partial t^2} &= \frac{1}{J} \frac{\partial}{\partial r_j} \left(J \frac{\partial r_j}{\partial x_k} \sigma_{ki} \right) + \rho_0 f_i, \\ \sigma_{ij} &= \lambda \epsilon_{kk} \delta_{ij} + 2\mu \epsilon_{ij}, \\ \epsilon_{ij} &= \frac{1}{2} \left(\frac{\partial r_k}{\partial x_j} \frac{\partial u_i}{\partial r_k} + \frac{\partial r_k}{\partial x_i} \frac{\partial u_j}{\partial r_k} \right),\end{aligned}$$

where $J = \det(\partial \mathbf{x} / \partial \mathbf{r})$ is the Jacobian of the mapping. These equations can be written succinctly as

$$\rho_0 \frac{\partial^2 u_i}{\partial t^2} = \frac{1}{J} \frac{\partial}{\partial r_j} \left(A_{ijkl} \frac{\partial u_k}{\partial r_l} \right) + \rho_0 f_i. \quad (10)$$

The equations in (10) can be discretized to second-order accuracy using a compact stencil (stencil width of three in each direction). Equation (10) contains two types of terms, terms with a mixed second-order

derivative and terms with an unmixed second-order derivative. These two types of terms are approximated using

$$\frac{\partial}{\partial r_j} \left(a_i \frac{\partial u_k}{\partial r_j} \right) \approx D_{+j} \left((\mathcal{A}_{-j} a_i) D_{-j} u_{k,i}^n \right), \quad (11)$$

$$\frac{\partial}{\partial r_j} \left(a_i \frac{\partial u_k}{\partial r_l} \right) \approx D_{0j} \left(a_i D_{0l} u_{k,i}^n \right), \quad j \neq l, \quad (12)$$

where $u_{k,i}^n \approx u_k(\mathbf{x}_i, t^n)$, $t^n = n\Delta t$, and where D_{+j} , D_{-j} and D_{0j} are the usual forward, backward and central difference approximations in the j^{th} coordinate direction and \mathcal{A}_{-j} is the averaging operator. For example,

$$\begin{aligned} D_{+1} u_{k,i} &= (u_{k,i_1+1,i_2,i_3}^n - u_{k,i}^n) / (\Delta r_1), \\ D_{-2} u_{k,i} &= (u_{k,i}^n - u_{k,i_1,i_2-1,i_3}^n) / (\Delta r_2), \\ \mathcal{A}_{-3} u_{k,i} &= \frac{1}{2} (u_{k,i_1,i_2,i_3}^n + u_{k,i_1,i_2,i_3-1}^n). \end{aligned}$$

For second-order accuracy we discretize the equations in time with a centered scheme,

$$\frac{\partial^2 u_k}{\partial t^2} \approx \frac{u_{k,i}^{n+1} - 2u_{k,i}^n + u_{k,i}^{n-1}}{\Delta t^2}, \quad (13)$$

and evaluate the forcing term as $f_{k,i}^n = f_k(\mathbf{x}_i, t^n)$. By using these approximations, together with special one-sided approximations at traction boundaries, the overall scheme is stable, second-order accurate, non-dissipative and preserves a discrete approximation to the energy on a single curvilinear grid. See Appelö and Petersson [9] for further details.

The basic conservative scheme has no-dissipation. On an overlapping grid, the interpolation equations may introduce perturbations to the approximation that can cause instabilities as analyzed in Section 6. To damp this instability we either add an artificial dissipation or apply a high-order low-pass filter. The artificial dissipation term is added to the right hand side of equation (10). In continuous terms it takes the form

$$\mathcal{D}^{2d} \mathbf{u} = -\alpha_d (-h^2 \Delta)^d \frac{\partial \mathbf{u}}{\partial t},$$

where $\alpha_d \geq 0$ is a constant and h is some measure of the grid spacing. The actual discrete approximation is defined in terms of undivided differences

$$\mathcal{D}_h^{2d} \mathbf{u}_i^n = -\alpha_d \sum_{d=1}^{n_d} (-\Delta_{+d} \Delta_{-d})^d \left(\frac{\mathbf{u}_i^n - \mathbf{u}_i^{n-1}}{\Delta t} \right), \quad (14)$$

where $\Delta_{+d} = \Delta r_d D_{+d}$ and $\Delta_{-d} = \Delta r_d D_{-d}$ are the un-divided forward and backward difference operators, respectively. For a second-order approximation we can use a second-order dissipation $2d = 2$ or a fourth-order $2d = 4$. In many cases the choice $\alpha_d = O(1)$ ($\alpha_d = 1$ for example) will lead to a stable numerical solution. However in more difficult cases as discussed in section (6) it is necessary to increase the coefficient as the mesh is refined, $\alpha_d \propto 1/\Delta r$. For these difficult cases we have found that the use of a high-order filter is generally better (see Section 6.1.2). The high-order low-pass filter is applied to the grid function \mathbf{u}_i^n to obtain a new filtered solution $\mathbf{u}^{n,*}$

$$\mathbf{u}^{n,*} = \mathcal{F}_{2d}(\mathbf{u}_i^n), \quad (15)$$

$$\mathcal{F}_{2d}(\mathbf{u}_i^n) = \mathbf{u}_i^n - \beta_d \sum_{d=1}^{n_d} (-\Delta_{+d} \Delta_{-d})^d \mathbf{u}_i^n. \quad (16)$$

The filter can be applied every time step or every few time steps. The coefficient β_d can be chosen so that the filter eliminates the most oscillatory grid function $\mathbf{u}_i = (-1)^{i_1} (-1)^{i_2} (-1)^{i_3}$. This *plus-minus* wave is often the most unstable mode. In this case

$$\beta_d = \frac{1}{4^d n_d}.$$

If the filter is applied at every time step, then the error introduced is $O((\Delta r)^{2d}/\Delta t)$. Choosing a fourth-order filter, $2d = 4$ will retain the second-order accuracy of the scheme. We have found that a sixth-order filter,

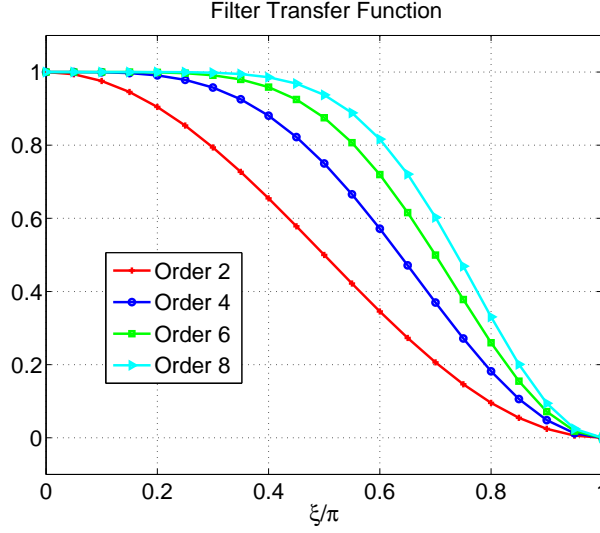


Fig. 2. Transfer function for the high-order filter. The plus-minus wave, which corresponds to $\xi/\pi = 1$, is completely damped by the filter.

$2d = 6$ is an even better choice since it is effective at stabilizing the scheme but results in little dissipation to the resolved modes of the computed solution. The fourth and sixth order filters require special treatment near boundaries due to their wide stencils. Rather than develop special one-sided approximations (as done for example in [10]) we instead assign values of the solution at extra ghost points. For the fourth-order filter we extrapolate \mathbf{u}_i^n on a second-ghost line to third-order (e.g. $D_{+j}^3 \mathbf{u}_i^n = 0$). On interpolation boundaries we also use third-order extrapolation to set values at the unused points that lie next to interpolation points. The sixth-order filter is implemented in two stages. In the first stage we extrapolate a second-ghost line to third-order and then evaluate and save $\mathbf{d}_i = (-\Delta_{+d}\Delta_{-d})^2 \mathbf{u}_i^n$. In the second stage we set \mathbf{d}_i to zero at ghost points and evaluate $\mathcal{F}_6(\mathbf{u}_i^n) = \mathbf{u}_i^n - \beta_6(-\Delta_{+d}\Delta_{-d})\mathbf{d}_i$. The Fourier transform of the one-dimensional filter (*transfer-function*) is shown in figure 2 and given by

$$\widehat{\mathcal{F}}_{2d}(\xi) = 1 - \sin^{2d}(\xi/2), \quad |\xi| \leq \pi, \quad (17)$$

where ξ is the normalized wave-number. It can be seen that the sixth order filter has little effect on the low frequency components of the solution while strongly damping the high frequencies. We note that another good filter might be the compact filters proposed by Lele and others [11].

4.2. First-order system

In this section, we consider a discretization of the first-order system of equations for elastic waves in n_d space dimensions. Let \mathbf{w} denote the vector of all dependent variables, $\mathbf{w} = [\mathbf{v} \ \boldsymbol{\sigma} \ \mathbf{u}]^T$. In Cartesian coordinates the FOS (8) can then be written in the form

$$\frac{\partial \mathbf{w}}{\partial t} + \sum_{\alpha=1}^{n_d} \frac{\partial}{\partial x_\alpha} (A^{(\alpha)} \mathbf{w}) = \mathbf{h}, \quad (18)$$

for matrices $A^{(\alpha)}$ which depend on ρ_0 , λ and μ and where $\mathbf{h} = \mathbf{h}(\mathbf{x}, t)$ denotes the forcing. We note that for variable coefficients, $\lambda(\mathbf{x})$ and $\mu(\mathbf{x})$, the forcing \mathbf{h} will also depend on \mathbf{w} . **Question: we don't need to deal with it here but I wonder how variable coefficients would be treated? The system could be put in conservation form plus a source term in which case $\mathbf{h} = \mathbf{h}(\mathbf{w}, \mathbf{x}, t)$.** As mentioned previously, each component grid in the overlapping grid is defined by a mapping $\mathbf{x} = \mathbf{G}(\mathbf{r})$. In computational space, \mathbf{r} , the equations (18) become

$$\frac{\partial}{\partial t} \mathbf{w} + \frac{1}{J} \sum_{\alpha=1}^{n_d} \frac{\partial}{\partial r_\alpha} \mathbf{f}^{(\alpha)}(\mathbf{w}) = \mathbf{h}, \quad (19)$$

$$\mathbf{f}^{(\alpha)}(\mathbf{w}) = J \left(\sum_{j=1}^{n_d} \frac{\partial r_\alpha}{\partial x_j} A^{(j)} \right) \mathbf{w}, \quad (20)$$

where $J = \det(\partial \mathbf{x} / \partial \mathbf{r})$ is the Jacobian of the mapping. The Jacobian and all grid metrics are assumed to be known smooth functions. The discretization of the mapped equations in (19) is performed on a uniform grid with mesh spacings Δr_α for $\alpha = 1 \dots n_d$. Following the approach discussed in [], **ref needed here** we use

$$\mathbf{w}_i^{n+1} = \mathbf{w}_i^n - \frac{\Delta t}{J_i} \sum_{\alpha=1}^{n_d} D_{+\alpha} \mathbf{f}_{i-\frac{1}{2}\hat{\mathbf{e}}_\alpha}^{(\alpha)} + \Delta t \mathbf{h}_i^{n+1/2}, \quad (21)$$

where \mathbf{w}_i^n is an approximation of \mathbf{w} at the grid point \mathbf{r}_i and time t_n , Δt is a global time step used for all grids at t_n , $\mathbf{f}_i^{(\alpha)}$ are numerical approximations to the fluxes defined in (20), $\mathbf{h}_i^{n+1/2}$ is an approximation to the source term, and $\hat{\mathbf{e}}_\alpha \in \mathbb{R}^{n_d}$ is the unit vector in the α -direction. For use below, define the shift operator in the α -direction, E_α , by $E_\alpha^\beta \mathbf{w}_i = \mathbf{w}_{i+\beta\hat{\mathbf{e}}_\alpha}$.

There are many possible choices for the numerical fluxes in (20). For nonlinear systems the exact Godunov flux can be expensive to compute. However, for the case of linear elasticity, the exact Godunov flux requires only the solution to a small linear system, which is computationally efficient, and so we use it. For the α -direction in index space this flux is given by

$$\mathbf{f}_{i+\frac{1}{2}\hat{\mathbf{e}}_\alpha}^{(\alpha)} = \frac{1}{2} \left(\mathbf{f}^{(\alpha)}(\mathbf{w}_R) + \mathbf{f}^{(\alpha)}(\mathbf{w}_L) \right) - E_\alpha^{\frac{1}{2}} \left[\frac{J_i}{2} \sum_{m=1}^{n_c} \Gamma_{\alpha,i}^{(m)} |K_{\alpha,i}^{(m)}| \mathbf{z}_{\alpha,i}^{(m)} \right], \quad (22)$$

where $(K_\alpha^{(m)}, \mathbf{z}_\alpha^{(m)})$, $m = 1, 2, \dots, n_c$, are the eigenvalues and eigenvectors belonging to the matrix

$$C_\alpha = Z_\alpha K_\alpha Z_\alpha^{-1} = \sum_{j=1}^{n_d} \frac{\partial r_\alpha}{\partial x_j} A^{(j)},$$

$\Gamma_\alpha^{(m)}$ is the m^{th} component of the vector $Z_\alpha^{-1}(\mathbf{w}_R - \mathbf{w}_L)$, and $n_c = 2n_d + n_d^2$ is the number of components in the solution vector \mathbf{w} . Values defined on the faces, $i + \frac{1}{2}\hat{\mathbf{e}}_\alpha$ are determined by averaging, for example, $J_{i+\frac{1}{2}\hat{\mathbf{e}}_\alpha} = \frac{1}{2}(J_{i+\hat{\mathbf{e}}_\alpha} + J_i)$. **(check me.)**

The numerical flux defined in (22) with left and right states taken directly from grid values on either side of a given cell face is in general first-order accurate. Second-order accuracy can be achieved (for smooth solutions) if modified values for the left and right states are used. For example, consider the cell face with index $i + \frac{1}{2}\hat{\mathbf{e}}_\alpha$ and define the vectors

$$\mathbf{a}_{\alpha,i}^n = \mathcal{L} \left(Z_{\alpha,i}^{-1} \Delta_{-\alpha} \mathbf{w}_i^n, Z_{\alpha,i}^{-1} \Delta_{+\alpha} \mathbf{w}_i^n \right), \quad (23)$$

where $\mathcal{L}(\cdot, \cdot)$ is a slope-limiter function which is applied componentwise. For the Euler equations of gas dynamics a common choice is the minmod (minimum modulus) limiter. For the current work, however, we use the unlimited scheme defined with $\mathcal{L}(b, c) = (b + c)/2$. The wave strengths in (23) are used to obtain the following values for the left and right states about the cell face $i + \frac{1}{2}\hat{\mathbf{e}}_\alpha$

$$\begin{aligned} \mathbf{w}_L &= \mathbf{w}_i^n + \frac{1}{2} Z_{\alpha,i} \mathbf{a}_{\alpha,i}^n - \sum_{j=1}^{n_d} \frac{\Delta t}{2\Delta r_j} Z_{j,i} K_{j,i} \mathbf{a}_{j,i}^n + \frac{\Delta t}{2} \mathbf{h}_i^n, \\ \mathbf{w}_R &= E_\alpha \left[\mathbf{w}_i^n - \frac{1}{2} Z_{\alpha,i} \mathbf{a}_{\alpha,i}^n - \sum_{j=1}^{n_d} \frac{\Delta t}{2\Delta r_j} Z_{j,i} K_{j,i} \mathbf{a}_{j,i}^n + \frac{\Delta t}{2} \mathbf{h}_i^n \right]. \end{aligned} \quad (24)$$

The values in (24) are used to compute $\mathbf{f}_{i+\frac{1}{2}\hat{\mathbf{e}}_\alpha}^{(\alpha)}$, and similar formulas give left and right states which may be used to compute the other numerical fluxes in (21). Finally, we note that the slope-limited wave strengths in (23) are also used to obtain the *center update*

$$\mathbf{w}_C^{n+\frac{1}{2}} = \mathbf{w}_i^n - \sum_{j=1}^{n_d} \frac{\Delta t}{2\Delta r_j} Z_{j,i} K_{j,i} \mathbf{a}_{j,i}^n + \frac{\Delta t}{2} \mathbf{h}_i^n. \quad (25)$$

The displacements are then advanced according to

$$\mathbf{u}_i^{n+1} = \mathbf{u}_i^n + \Delta t \mathbf{v}_C^{n+\frac{1}{2}}. \quad (26)$$

This completes the description of the numerical scheme for the first-order system.

5. Boundary Conditions

An important issue in the discretization of PDEs is the numerical treatment of boundary conditions. In this section, we describe our implementation of the boundary conditions (5)-(7) for the second-order and first-order systems.

The boundary conditions are applied after the solution has first been advanced at all interior and boundary points using the algorithm outlined previously in Sections 4.1 and 4.2. Note that the interior equations are advanced at boundary points, providing preliminary values of the solution on the boundary. Some of these boundary values will be over-written by the boundary conditions but some will not. To be specific, we consider applying the boundary conditions to the face, $r_1 = 0$ with $i_1 = 0$. Let $\mathbf{j} = (i_2, i_3)$ denote the indices for the tangential directions. We use the boundary conditions to assign appropriate values of the solution on the boundary, $\mathbf{u}_{0,\mathbf{j}}$, the first ghost line $\mathbf{u}_{-1,\mathbf{j}}$, and for the FOS-G scheme the second ghost line, $\mathbf{u}_{-2,\mathbf{j}}$.

5.1. Boundary conditions for the second-order system

The displacement boundary conditions (5) are straightforward to implement for the SOS, by setting

$$\mathbf{u}_i^n = \mathbf{g}_d(\mathbf{x}_i, t^n),$$

for all points \mathbf{i} on the boundary face. The values at ghost points, needed by the filter for e.g., are obtained by extrapolation, using the third-order extrapolation formula given in (28). The traction boundary conditions (6) require more care. We use the traction boundary conditions to assign values of the solution on the first ghost line $\mathbf{u}_{-1,\mathbf{j}}$. The values of the solution on the boundary are obtained using the interior equations. The traction boundary conditions define Neumann-like conditions on \mathbf{u} . For example, in the two-dimensional Cartesian case with a boundary on $x = 0$ these are

$$\begin{aligned} \frac{\partial u_1}{\partial x} &= -\frac{\lambda}{\lambda + 2\mu} \frac{\partial u_2}{\partial y}, \\ \frac{\partial u_2}{\partial x} &= -\frac{\partial u_1}{\partial y}. \end{aligned}$$

These conditions can be approximated with centered difference approximations and used to give equations for $\mathbf{u}_{-1,\mathbf{j}}$. We have found that these approximations will lead to an accurate scheme that is stable for moderate values of the ratio λ/μ but will generally be unstable for large values of this ratio. An approximation that is stable for all ratios can be determined by the summation-by-parts approach [12] which leads to a scheme with an energy estimate. The conclusion is that the centered approximation (12) to the mixed derivatives

$$\frac{\partial}{\partial r_j} \left(a_i \frac{\partial u_k}{\partial r_l} \right) \approx D_{0j} \left(a_i D_{0l} u_{k,i}^n \right), \quad j \neq l,$$

should be changed at the boundary $i_1 = 0$ by replacing the centered operator D_{01} by the one-sided operator D_{+1} . This change, together with centered approximations to the traction conditions (6), will give a stable, second-order accurate, self-adjoint scheme. See [9] for full details.

The slip-wall boundary condition (7) combines aspects of the displacement and traction boundary conditions. The normal component of the displacement is given on the boundary,

$$\mathbf{n} \cdot \mathbf{u}_i^n = \mathbf{n} \cdot \mathbf{g}_d(\mathbf{x}_i, t^n).$$

The tangential components of the traction boundary condition define $n_d - 1$ Neumann-like equations for the tangential components of the displacement on the ghost line. The normal component of the displacement on the ghost line is extrapolated .

5.2. Boundary conditions for the first-order system

Application of the boundary conditions for the first-order-system is somewhat more involved than for the second-order system due to the increased number of dependent variables. Let \mathbf{w} denote the vector of all dependent variables, $\mathbf{w} = [\mathbf{v} \ \boldsymbol{\sigma} \ \mathbf{u}]^T$ and denote the stress-strain relation by

$$\boldsymbol{\sigma} = \mathcal{S}(\nabla \mathbf{u}) = \lambda \nabla \cdot \mathbf{u} + \mu (\nabla \mathbf{u} + \nabla \mathbf{u}^T). \quad (27)$$

There are three types of conditions we apply. The first type are the analytic boundary conditions such as $\mathbf{u}_{0,j} = \mathbf{g}_d$. The second type are compatibility conditions that are derived from the governing equations and the boundary conditions. An example of a compatibility condition is $\nabla_h \cdot \boldsymbol{\sigma}_{0,j} = \rho \ddot{\mathbf{g}}_d$ which is derived from the governing equation (1) and the analytic boundary condition (5). The third type are extrapolation conditions. We use a third-order extrapolation operator given by

$$\mathbf{w}_{-1,j} = \mathcal{E}_{+1}^{(3)} \mathbf{w}_{0,j} = 3\mathbf{w}_{0,j} - 3\mathbf{w}_{1,j} + \mathbf{w}_{2,j}. \quad (28)$$

Displacement boundary condition		
stage	condition	assigns
1a	$\mathbf{u}_{0,j} = \mathbf{g}_d$	$\mathbf{u}_{0,j}$
1b	$\mathbf{v}_{0,j} = \dot{\mathbf{g}}_d$	$\mathbf{v}_{0,j}$
2	Extrapolate $\mathbf{w}_{-1,j}$	$\mathbf{w}_{-1,j}$
3	$\nabla_h \cdot \boldsymbol{\sigma}_{0,j} = \rho \ddot{\mathbf{g}}_d$	$\mathbf{n} \cdot \boldsymbol{\sigma}_{-1,j}$
4	Extrapolate $\mathbf{w}_{-2,j}$	$\mathbf{w}_{-2,j}$

Traction boundary condition		
stage	condition	assigns
1	$\mathbf{n} \cdot \boldsymbol{\sigma}_{0,j} = \mathbf{g}_t$	$\mathbf{n} \cdot \boldsymbol{\sigma}_{0,j}$
2	Extrapolate $\mathbf{w}_{-1,j}$	$\mathbf{w}_{-1,j}$
3a	$\mathbf{n} \cdot \mathcal{S}(\nabla_h \mathbf{u}_{0,j}) = \mathbf{g}_t$	$\mathbf{u}_{-1,j}$
3b	$\mathbf{n} \cdot \mathcal{S}(\nabla_h \mathbf{v}_{0,j}) = \dot{\mathbf{g}}_t$	$\mathbf{v}_{-1,j}$,
4	$\boldsymbol{\tau}_m \cdot \boldsymbol{\sigma}_{0,j} = \boldsymbol{\tau} \cdot \mathcal{S}(\nabla_h \mathbf{u}_{0,j})$	$\boldsymbol{\tau}_m \cdot \boldsymbol{\sigma}_{0,j}$
5	Extrapolate $\boldsymbol{\sigma}_{-1,j}$	$\boldsymbol{\sigma}_{-1,j}$
6	Extrapolate $\mathbf{w}_{-2,j}$	$\mathbf{w}_{-2,j}$

Slip wall boundary condition		
stage	condition	assigns
1a	$\mathbf{n} \cdot \mathbf{u}_{0,j} = g_s$	$\mathbf{n} \cdot \mathbf{u}_{0,j}$
1b	$\mathbf{n} \cdot \mathbf{v}_{0,j} = \dot{g}_n$	$\mathbf{n} \cdot \mathbf{v}_{0,j}$
1c	$\mathbf{n} \cdot \boldsymbol{\sigma}_{0,j} \cdot \boldsymbol{\tau}_m = g_{s,m}$	$\mathbf{n} \cdot \boldsymbol{\sigma}_{0,j} \cdot \boldsymbol{\tau}_m$
2	Extrapolate $\mathbf{w}_{-1,j}$	$\mathbf{w}_{-1,j}$
3a	$\mathbf{n} \cdot \mathcal{S}(\nabla_h \mathbf{u}_{0,j}) \cdot \boldsymbol{\tau}_m = g_{t,m}$	$\boldsymbol{\tau}_m \cdot \mathbf{u}_{-1,j}$
3b	$\mathbf{n} \cdot \mathcal{S}(\nabla_h \mathbf{v}_{0,j}) \cdot \boldsymbol{\tau}_m = \dot{g}_{t,m}$	$\boldsymbol{\tau}_m \cdot \mathbf{v}_{-1,j}$,
3c	$\boldsymbol{\sigma}_{0,j} = \mathcal{S}(\nabla_h \mathbf{u}_{0,j})$	$\boldsymbol{\sigma}_{0,j}$
5	Extrapolate $\boldsymbol{\sigma}_{-1,j}$	$\boldsymbol{\sigma}_{-1,j}$
6	Extrapolate $\mathbf{w}_{-2,j}$	$\mathbf{w}_{-2,j}$

Table 1

Implementation of the displacement, traction and slip-wall boundary conditions for the first-order-system. The values of the solution on the boundary and ghost points are assigned in the order given.

Table 1 outlines the steps we take (in the order given) to apply the discrete versions of the boundary conditions. Consider, for example, the condition $\nabla_h \cdot \boldsymbol{\sigma}_{0,j} = \rho \ddot{\mathbf{g}}_d$ from stage 3 of the displacement boundary condition. This equation is discretized to second-order-accuracy using the conservative approximation,

$$\nabla_h \cdot \boldsymbol{\sigma}_i = \frac{1}{J_i} \sum_{m=1}^{n_d} D_{0,m} \left(\nabla_{\mathbf{x}} r_m \cdot \boldsymbol{\sigma}_i \right) = \rho \ddot{\mathbf{g}}_d,$$

centered on the boundary point $\mathbf{i} = (0, \mathbf{j})$. These n_d equations can be solved for the n_d values $\mathbf{n} \cdot \boldsymbol{\sigma}_{-1, \mathbf{j}}$ of the normal dotted with the stress on the ghost points (note that $\mathbf{n} = \nabla_{\mathbf{x}} r_1 / |\nabla_{\mathbf{x}} r_1|$). The values of $\boldsymbol{\sigma}_{-1, \mathbf{j}}$ are then adjusted so that these conditions are satisfied.

6. Stability at overlapping grid interfaces with nearby boundaries

In this section we analyze some aspects of the stability of our schemes on overlapping grids. A numerical scheme that is stable on a single grid may become unstable on an overlapping grid. This is especially a problem for neutrally stable schemes that have no dissipation. In practice we often have a narrow curvilinear grid next to boundaries. As the boundary grid is refined we may keep fixed the number of grid points, N , in the normal direction to the boundary. This can be useful from an efficiency standpoint as the relative number of grid points on the more efficient Cartesian grids will grow. We will see that the case of fixed N is more difficult than the case of increasing N since instabilities generated from the interpolation equations at grid overlaps can be made worse by the presence of a nearby boundary.

The equations of linear elasticity are a coupled set of wave equations. As a model problem we consider the solution to a scalar wave equation in one-dimension. We study both the second-order wave equation and the first-order wave equation. We analyze approximations to these equations on a one-dimensional overlapping grid. We show that non-dissipative centered approximations are unstable for certain values of the overlap parameters (e.g., interpolation coefficients) and that the growth rates of these unstable modes increase as the mesh is refined. The centered schemes can be stabilized with artificial dissipation provided the coefficient of the artificial dissipation also increases as the mesh is refined. The Godunov scheme for the first-order wave equation is found to have enough inherent dissipation to be stable without requiring any additional dissipation.

The stability of hyperbolic problems on overlapping grids has been previously considered by various authors. The case of adaptive mesh refinement, a special case of an overlapping grid, has been considered by, for example, Browning, Kreiss and Oliger [13] and Ciment [14]. Berger [15] considered the stability of the first order wave equation with mesh refinement in space and time. Starius [16] studied the stability of the Lax-Wendroff scheme for the first order wave equation on a semi-infinite one-dimensional overlapping grid. Reyna [17] also analyzed the first order wave equation on an overlapping grid and showed that the leap-frog scheme could be unstable. Pärt-Enander and Sjögreen [18] considered the stability of conservative interpolation on overlapping grids. Olsson and Peterson [19] studied the first-order wave equation and showed the existence of a whole class of unstable modes. They also demonstrated numerically that the growth rates of the unstable modes increased as the mesh was refined, although quite slowly.

We extend these previous works to the case of the second-order wave equation and also present some new results for the first-order wave equation. We analyze in particular the case when the number of points, N , in the boundary grid remains fixed as the mesh is refined and show that the growth rate of unstable modes increases proportional to $1/h$ where h is the mesh size.

6.1. Stability of the second-order wave equation

We consider solving the second-order scalar wave equation in one space dimension for the unknown $u = u(x, t)$ on the semi-infinite interval $\Omega = (-\infty, b]$,

$$\begin{aligned} \frac{\partial^2 u}{\partial t^2} &= \frac{\partial^2 u}{\partial x^2}, & x \in (\infty, b), \quad t > 0, \\ u(x, 0) &= u_0(x), & x \in (\infty, b), \\ u(b, t) &= g(t), \quad \|u(\cdot, t)\| < \infty, & t > 0. \end{aligned}$$

Here the initial and boundary conditions are assumed consistent so that $u_0(b) = g(0)$. We solve this equation on an overlapping grid for the semi-infinite interval is shown in Fig. 3. The solution is approximated by the two grid functions $u_j^{(m)}(t) \approx u(x_j^{(m)}, t)$, on the component grids $x_j^{(m)} = x_a^{(m)} + jh_m$, for $m = 1, 2$. The grid spacings are $h_m > 0$ and let $h = \min(h_1, h_2)$. This overlapping grid is representative of the grids we generally use where there is a narrow boundary fitted grid with a fixed number of grid points in the direction normal to the boundary (i.e. N is constant as the mesh is refined) next to a large background grid.

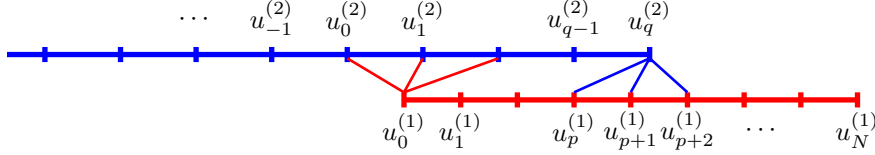


Fig. 3. One-dimensional overlapping grid for the semi-infinite problem.

We consider approximations that are continuous in time and discrete in space. A centered approximation is

$$\frac{\partial^2 u_j^{(1)}}{\partial t^2} = \frac{u_{j+1}^{(1)} - 2u_j^{(1)} + u_{j-1}^{(1)}}{h_1^2}, \quad j = 1, 2, 3, \dots, N-1 \quad (29)$$

$$\frac{\partial^2 u_j^{(2)}}{\partial t^2} = \frac{u_{j+1}^{(2)} - 2u_j^{(2)} + u_{j-1}^{(2)}}{h_2^2}, \quad j = q-1, q-2, \dots \quad (30)$$

with initial conditions and boundary conditions

$$u_j^{(1)} = u_0(x_j^{(1)}), \quad j = 0, 1, 2, 3, \dots, N, \quad (31)$$

$$u_j^{(2)} = u_0(x_j^{(1)}), \quad j = q, q-1, q-2, \dots, \quad (32)$$

$$u_N^{(1)} = g(t), \quad (33)$$

and interpolation conditions,

$$u_0^{(1)} = \sum_{k=0}^r a_k u_k^{(2)}, \quad u_q^{(2)} = \sum_{k=0}^r b_k u_{p+k}^{(1)}. \quad (34)$$

Here $r+1$ is the number of points in the interpolation stencil. The interpolation coefficients a_k and b_k are given by Lagrange interpolation, where for example,

$$\begin{aligned} a_0 &= (1 - \alpha), \quad a_1 = \alpha, & (\text{linear interpolation, } r = 1), \\ a_0 &= \frac{1}{2}(1 - \alpha)(2 - \alpha), \quad a_1 = \alpha(2 - \alpha), \quad a_2 = \frac{1}{2}\alpha(\alpha - 1), & (\text{quadratic interpolation, } r = 2), \\ \alpha &= (x_0^{(1)} - x_0^{(2)})/h_2. \end{aligned}$$

The interpolation is restricted to be centered so that $\alpha \in [\frac{1}{2}(r-1), \frac{1}{2}(r+1)]$. The formulae for b_k are defined in a similar fashion in terms of $\beta = (x_q^{(2)} - x_p^{(1)})/h_1$.

Definition 1 *We will say that the solution to scheme (29)-(34) is stable if the solutions remain uniformly bounded in time.*

We note that more generally one can allow stable solutions that have bounded growth in time for any fixed time interval, but for the wave equation this more restrictive definition will be used. To analyze the stability of this approximation, we Laplace transform in time with dual variable s . From the general normal-mode theory [12] we are led to analyze the following eigenvalue problem for the semi-discrete, Laplace transformed solution,

$$(sh_1)^2 \tilde{u}_j^{(1)} = \tilde{u}_{j+1}^{(1)} - 2\tilde{u}_j^{(1)} + \tilde{u}_{j-1}^{(1)}, \quad j = 1, 2, 3, \dots, N-1, \quad (35)$$

$$(sh_2)^2 \tilde{u}_j^{(2)} = \tilde{u}_{j+1}^{(2)} - 2\tilde{u}_j^{(2)} + \tilde{u}_{j-1}^{(2)}, \quad j = q-1, q-2, \dots, \quad (36)$$

$$\tilde{u}_N^{(1)} = 0, \quad |\tilde{u}_j^{(2)}| < \infty, \quad (37)$$

$$\tilde{u}_0^{(1)} = \sum_{k=0}^r a_k \tilde{u}_k^{(2)}, \quad \tilde{u}_q^{(2)} = \sum_{k=0}^r b_k \tilde{u}_{p+k}^{(1)}. \quad (38)$$

A necessary condition for stability, known as the Godunov-Ryabenkii condition, is that there be no solutions to the eigenvalue problem with $Re(s) > 0$ as indicated by the following theorem.

Theorem 1 *The scheme (29)-(34) is unstable if there exist solutions to the eigenvalue problem (35)-(38) with $Re(s) > 0$.*

Proof. If there is a solution to the eigenvalue problem (35)-(38) then there will be a homogeneous solution to (29)-(34) which grows like e^{st} . If $Re(s) > 0$ this solution will not be bounded in time \square .

The next lemma follows from the fact that the eigenvalue problem only depends on the product sh_m .

Lemma 1 *If there is a solution to the eigenvalue problem (35)-(38) for given values $(s, h_1, h_2, \alpha, \beta, N)$, then for any $\gamma > 0$ there will be another solution (on a different grid) with values $(s\gamma, h_1/\gamma, h_2/\gamma, \alpha, \beta, N)$.*

The growth rate on the new grid will be $e^{\gamma Re(s)t}$. Therefore if there exists a solution to the eigenvalue problem with $Re(s) > 0$ then we can find solutions on finer grids that grow more rapidly. This result indicates that if there are unstable modes for one mesh size then as the mesh is refined there will be unstable modes with growth rates proportional to $1/h_m$, i.e., $|u_j^{(m)}| \sim e^{(\gamma/h_m)t}$, with $\gamma > 0$.

To solve equations (35) and (36) we make the ansatz $\tilde{u}_j^{(m)} = C_m(s)\kappa^j$ for some bounded and spatially constant $C_m(s)$. It follows that κ will satisfy

$$\kappa^2 - (2 + (sh_m)^2)\kappa + 1 = 0$$

with roots

$$\kappa_{\pm} = 1 + z/2 \pm \sqrt{z + z^2/4}$$

where $z = (sh_m)^2$. When investigating stability we are interested in the root $\kappa^* = \kappa^*(sh)$ with $|\kappa^*| \leq 1$ for $Re(s) > 0$. If $sh = \xi + i\eta$, $\xi, \eta \in \mathbb{R}$, then this root is given by

$$\kappa^*(sh) = \begin{cases} 1 + z/2 - \sqrt{z + z^2/4}, & \text{for } \eta^2 \leq \xi^2 + 2, \\ 1 + z/2 + \sqrt{z + z^2/4}, & \text{for } \eta^2 > \xi^2 + 2, \end{cases} \quad (39)$$

$$-\pi/2 \leq \arg(\sqrt{z + z^2/4}) < \pi/2. \quad (40)$$

This last equation is valid for $\xi > 0$ (the correct branch cut for $\xi = 0$ must be obtained from $\xi \rightarrow 0$, $\xi > 0$). The modulus of this root is plotted in Fig. 4. Note that $|\kappa^*(sh)| = 1$ for $sh = i\eta$ with $-2 \leq \eta \leq 2$. Also note that $\kappa^*(sh) \sim 1/z$ as $z \rightarrow \infty$ with $Re(s) > 0$.

The solution to equations (35) and (36) satisfying the boundary conditions is thus of the form

$$\begin{aligned} \tilde{u}_j^{(1)} &= A(\kappa_1^j - \kappa_1^{2N-j}), \quad j = 0, 1, 2, \dots, N \\ \tilde{u}_j^{(2)} &= B\kappa_2^{q-j}, \quad j = q, q-1, q-2, \dots, \end{aligned}$$

where $\kappa_m = \kappa^*(sh_m)$, $m = 1, 2$, are the roots with $|\kappa_m| \leq 1$ for $Re(s) > 0$ (see equation 39). Imposition of the interpolation equations implies

$$\begin{aligned} A(1 - \kappa_1^{2N}) &= B \sum_{k=0}^r a_k \kappa_2^{q-k}, \\ B &= A \sum_{k=0}^r b_k \left(\kappa_1^{p+k} - \kappa_1^{2N-(p+k)} \right). \end{aligned}$$

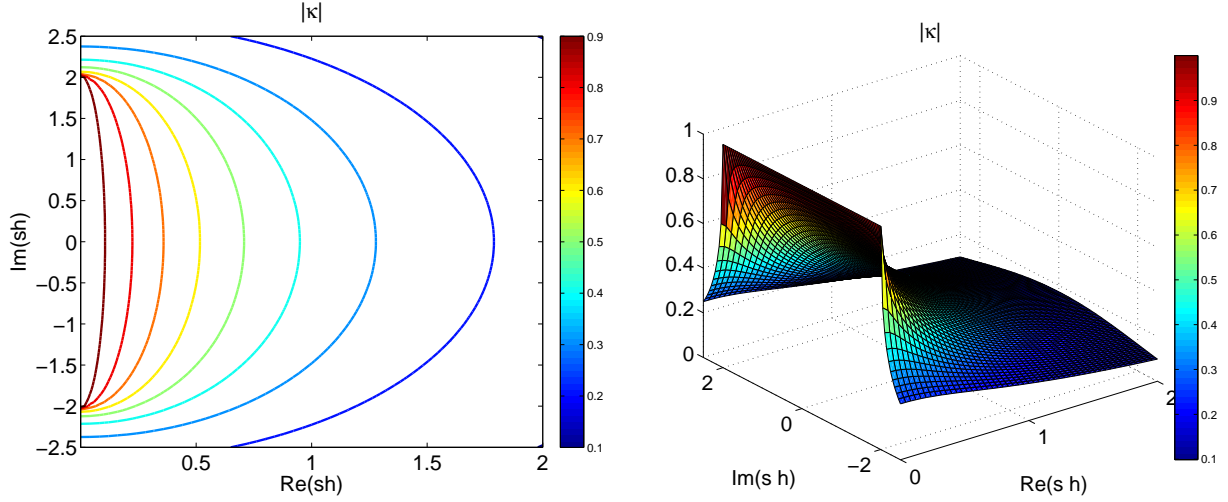


Fig. 4. Contours and surface plot of $|\kappa|$ from the second-order wave equation for the root $\kappa^*(sh)$ with $|\kappa| \leq 1$ for $Re(s) > 0$. The modulus of κ^* is one along the imaginary axis for $Im(sh) \in [-2, 2]$ and decays to zero as $Re(sh) \rightarrow \infty$.

The condition for non-trivial solutions is that there be zeros of the following determinant for $Re(s) > 0$,

$$G_s = \det \begin{bmatrix} \kappa_1^{2N} - 1 & \sum_{k=0}^r a_k \kappa_2^{q-k} \\ \sum_{k=0}^r b_k (\kappa_1^{p+k} - \kappa_1^{2N-(p+k)}) & -1 \end{bmatrix}.$$

Whence

$$\begin{aligned} G_s(s) &= 1 - \kappa_1^{2N} - \left(\sum_{k=0}^r a_k \kappa_2^{q-k} \right) \left(\sum_{k=0}^r b_k (\kappa_1^{p+k} - \kappa_1^{2N-(p+k)}) \right) \\ &= 1 - \kappa_1^{2N} - \left(\sum_{k=0}^r a_k \kappa_2^{r-k} \right) \left(\sum_{k=0}^r b_k (\kappa_1^k - \kappa_1^{2N-2p-k}) \right) \kappa_2^{q-r} \kappa_1^p \end{aligned} \quad (41)$$

We will show shortly that there are, in general, solutions to $G_s(s) = 0$ with $Re(s) > 0$. We first prove,

Lemma 2 *The growth-rate of solutions to the eigenvalue problem with $G_s(s) = 0$, are bounded by $e^{(\gamma/h)t}$ where $\gamma = \gamma(r) \geq 0$ is a bounded constant that only depends on r .*

Proof. Note that $|\kappa_m(sh_m)| \rightarrow 0$ as $Re(s) \rightarrow \infty$. Thus for any $\epsilon > 0$ we can find $\gamma > 0$ such that $|\kappa_m| < \epsilon$ for $Re(sh) > \gamma$. Here γ does not depend on h . For example, from Fig. 4 we see that $|\kappa_m(sh_m)| < \frac{1}{2}$ for $Re(sh_m) > 1$. Assuming $2N - 2p - r \geq 0$ and $p + q > r$, and using $|\kappa_m| < \epsilon \leq 1$ it follows that

$$\begin{aligned} \left| \left(\sum_{k=0}^r a_k \kappa_2^{r-k} \right) \left(\sum_{k=0}^r b_k (\kappa_1^k - \kappa_1^{2N-2p-k}) \right) \kappa_2^{q-r} \kappa_1^p \right| &\leq \left(\sum_{k=0}^r |a_k| \right) 2 \left(\sum_{k=0}^r |b_k| \right) |\kappa_2|^{q-r} |\kappa_1|^p \\ &< 2 C_r^2 \epsilon^{p+q-r} \end{aligned}$$

where

$$C_r = \max_{-\frac{1}{2} \leq \alpha - r/2 \leq \frac{1}{2}} \sum_{k=0}^r |a_k(\alpha)|.$$

For example, for linear interpolation, $C_1 = 1$, while for quadratic interpolation $C_2 = 5/4$. We can thus choose ϵ small enough so that $\epsilon^{2N} < \frac{1}{2}$ and $2 C_r^2 \epsilon^{p+q-r} < \frac{1}{2}$ and thus $|G_s(s)| > 0$. This proves the lemma \square .

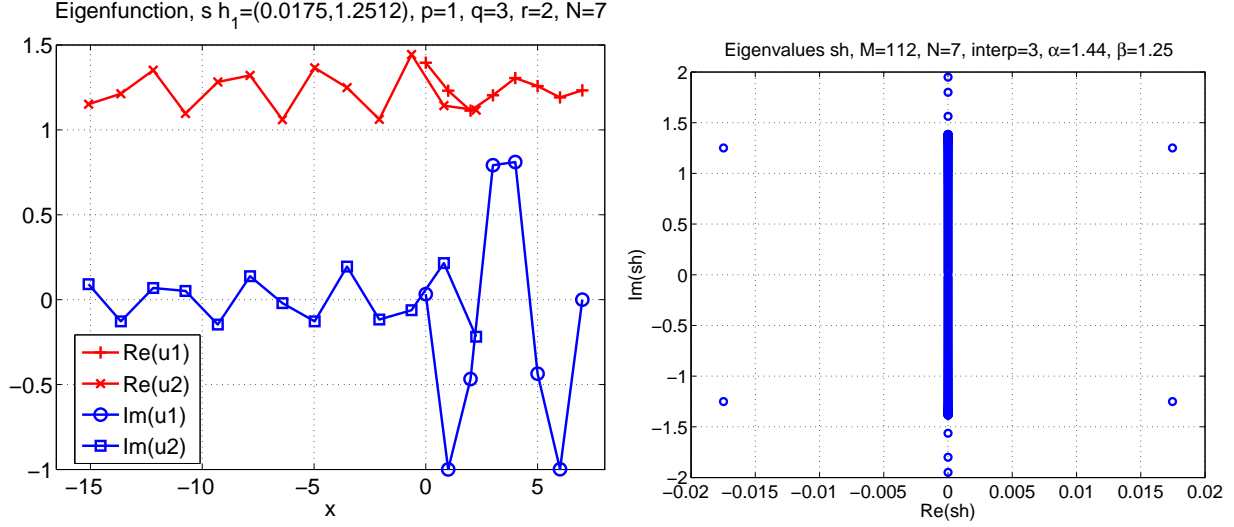


Fig. 5. Second-order wave equation. Left: Overlapping grid eigenfunction for the unstable mode $s \approx (0.01747, 1.251)$, $N = 7$ on the semi-infinite interval. The real part of the eigenfunction has been shifted upward for clarity. Right: The eigenvalues s of the finite domain overlapping grid problem with $N = 7$ and $M = 112$. The finite domain problem has a complex eigenvalue $s \approx (0.01747, 1.251)$ which agrees with that of the semi-infinite domain value.

Note: For the case of an infinite interval, $N \rightarrow \infty$, and linear interpolation it is not hard to show that there are no solutions with $Re(s) > 0$ but that there are solutions $Re(s) = 0$ and $|\kappa_m| = 1$. These latter solutions are called generalized eigenvalues. For quadratic interpolation on the infinite interval there are also generalized eigenvalues with $Re(s) = 0$ but we do not know whether there exist any roots with $Re(s) > 0$.

Note: (todo?) We should also be able to show that there are no roots for $sh \ll 1$ except for the case $s = 0$. This implies we only need to add dissipation to high-frequency modes.

6.1.1. Example of an unstable mode for the second-order wave equation

For a given grid with overlap parameters $(h_1, h_2, \alpha, \beta, p, q, N)$ there may or may not be a solution to $G_s(s) = 0$ with $Re(s) > 0$. A search of the parameter space can be used to locate solutions. Here is an example of an unstable solution with a relatively large value for $Re(s)$ that arises on an overlapping grid with overlap parameters that are typical of grids used in practice. For the overlap parameters

$$(h_1 = 1, h_2 \approx 1.4445, x_q^{(2)} - x_0^{(1)} \approx 2.2524, p = 1, q = 3, \alpha \approx 1.4408, \beta \approx 1.2527, N = 7) \quad (42)$$

we numerically find the root of $G_s(s) = 0$ to be $sh_1 \approx (0.01747, 1.251)$. The real and imaginary parts of the eigenfunction are shown in Fig. 5. Note that the imaginary parts of the eigenfunctions have opposite curvatures in the overlap region and do not match well there. This bad behaviour seems to be typical of unstable modes.

We can also compute all the eigenvalues of the matrix of the related finite interval problem where we truncate the interval on the left and choose the boundary condition $\tilde{u}_{q-M}^{(2)} = 0$. Using the same overlap parameters (42) we find that the finite domain problem has a complex eigenvalue that converges to the eigenvalue of the semi-infinite domain as M gets large. For example, for $M = 112$, the eigenvalues of the finite domain problem are shown in Fig. 5 and there is a complex eigenvalue $s \approx (0.01747, 1.251)$ which agrees with the results of the infinite domain value to the number of digits given.

6.1.2. Artificial dissipation and high-order filtering

We can stabilize the scheme (29)-(34) by adding an artificial dissipation of the form

$$\frac{\partial^2 u}{\partial t^2} = c^2 \frac{\partial^2 u}{\partial x^2} - c \frac{a_d}{h} \left(-h^2 \frac{\partial^2}{\partial x^2} \right)^d \partial_t u,$$

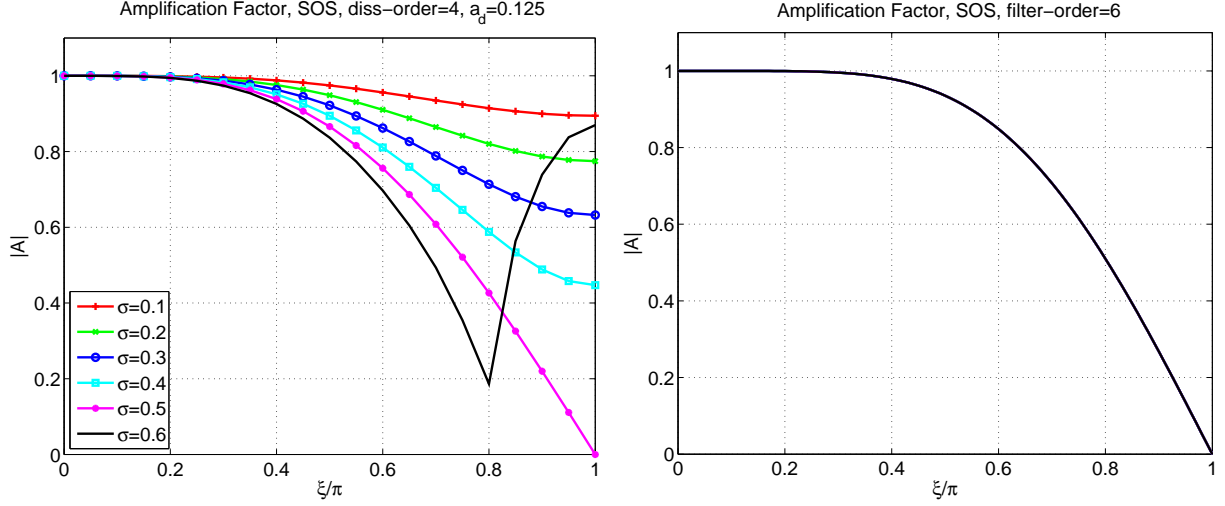


Fig. 6. The magnitude of the amplification factor as a function of $\sigma = c\Delta t/h$ and the normalized wave-number, ξ/π , for the SOS scheme for the one-dimensional second-order wave equation on a periodic domain. Left: SOS scheme with a fourth-order artificial dissipation. Right: SOS scheme with a sixth-order filter. The magnitude of the amplification factor for the filter scheme is independent of σ .

for some positive integer $d = 1, 2, \dots$, where we have included the wave speed $c > 0$ for clarity. The fully discrete approximation is

$$\frac{u_i^{n+1} - 2u_i^n + u_i^{n-1}}{\Delta t^2} = c^2 \frac{u_{j+1}^n - 2u_j^n + u_{j-1}^n}{h^2} - c \frac{a_d}{h} (-\Delta_+ \Delta_-)^d \frac{u_i^n - u_i^{n-1}}{\Delta t}, \quad (43)$$

or

$$u_i^{n+1} = 2u_i^n - u_i^{n-1} + \sigma^2(u_{j+1} - 2u_j + u_{j-1}) - \sigma a_d (-\Delta_+ \Delta_-)^d (u_i^n - u_i^{n-1}), \quad (44)$$

where $\sigma = c\Delta t/\Delta x$. Note that the discrete scheme depends on Δt and h only through σ and thus the dissipation only depends on σ as the mesh is refined. We say that the coefficient of dissipation increases like $1/h$ from its form in (43). The factor of $1/h$ is not needed for weaker instabilities where the growth rate remains bounded as h goes to zero. The symbol or amplification factor, \mathcal{A}_d for the scheme on a periodic domain is obtained by substituting $u_i^n = \mathcal{A}_d^n e^{ij\xi}$ into (44) giving a quadratic equation for $\mathcal{A}_d = \mathcal{A}_d(\xi, \sigma)$,

$$\mathcal{A}_d^2 = (2 - 4\sigma^2 \sin^2(\xi/2) - \sigma a_d (4 \sin^2(\xi/2))^d) \mathcal{A}_d - (1 - \sigma a_d (4 \sin^2(\xi/2))^d) \quad (45)$$

where $|\xi| \leq \pi$. Fig. 6 shows $|\mathcal{A}_d|$ for a case of fourth-order dissipation, $d = 2$ with $a_d = 1/8$ for various values of σ . The magnitude of the amplification factor, $|\mathcal{A}_d|$, indicates how much each Fourier mode is damped per time step. With no dissipation, $a_d = 0$, and $\sigma \leq 1$, $|\mathcal{A}_d| = 1$ for all ξ . For $a_d > 0$ the scheme is stable and there is damping of the high frequencies provided $\sigma < \sigma_0$ where the stability bound σ_0 depends on a_d and d . The figure shows that for the given parameters, where $\sigma_0 \approx .617$, the value of $\sigma = \frac{1}{2}$ results in the highest frequency on the mesh (the plus-minus wave) being completely damped. For $\sigma = .6$ there is less damping of the high frequencies and for $\sigma > \sigma_0$ the scheme is unstable and the high-frequencies are amplified.

The high-order filter, discussed in section 4.1, provides another way to add dissipation. The fully discrete scheme is a two step process,

$$u_i^* = 2u_i^n - u_i^{n-1} + \sigma^2(u_{j+1} - 2u_j + u_{j-1}), \quad (46)$$

$$u_i^{n+1} = u_i^* - a_f (-\Delta_+ \Delta_-)^d u_i^*. \quad (47)$$

The amplification factor for this scheme on a periodic domain is

$$\mathcal{A}_f^2 = \mathcal{T}_f [(2 - 4\sigma^2 \sin^2(\xi/2)) \mathcal{A}_f - 1], \quad (48)$$

$$\mathcal{T}_f = 1 - a_f (4 \sin^2(\xi/2))^d, \quad (49)$$

where \mathcal{T}_f is the transfer function for the filter. If Δt is chosen so that the unfiltered scheme is stable, $|\sigma| \leq 1$, then the filtered scheme satisfies

$$|\mathcal{A}_f| = |\mathcal{T}_f|. \quad (50)$$

Provided $|\mathcal{T}_f| \leq 1$, the filtered scheme (46)-(47) will be stable under the same time-step restriction as the unfiltered scheme. The filtered-scheme would therefore seem superior to the artificial dissipation scheme since it does not require the time-step to be reduced and its damping characteristics do not depend on σ . Fig. 6 shows the magnitude of the amplification factor for the sixth-order filter, $d = 3$, with $a_f = 1/2^{2d}$.

We now describe how the filter can stabilize the solution. Consider the situation when the scheme without dissipation has an unstable mode of the form

$$u_j^n \approx e^{s(n\Delta t)} \kappa^j = e^{s_r(n\Delta t)} e^{is_i n\Delta t} |\kappa|^j e^{ij\xi}, \quad (51)$$

where $s = (s_r, s_i)$ has a real part $s_r > 0$ and $\xi = \arg(\kappa)$, $|\xi| \leq \pi$. At each time step this solution will grow by a factor

$$\mathcal{A} = e^{s_r \Delta t} = e^{(s_r h) \sigma} \approx 1 + (s_r h) \sigma, \quad (52)$$

where $\sigma = \Delta t/h$. The filtered scheme will have an amplification per time step of

$$\mathcal{A}_f = \mathcal{T}_f(\xi) e^{(s_r h) \sigma} = (1 - a_f (4 \sin^2(\xi/2))^d) e^{(s_r h) \sigma}. \quad (53)$$

Recall that $s_r h$ remains bounded as $h \rightarrow 0$. The filtered scheme will be stable provided $|\mathcal{T}_f(\xi) e^{(s_r h) \sigma}| \leq 1$. For $\xi \neq 0$, $|\xi| \leq \pi$, we can always stabilize the scheme for small enough σ since the filter does not depend on σ and $|\mathcal{T}_f(\xi)| < 1$. As an example, consider the unstable solution from section 6.1.1 with $s_r h_1 = .0175$, $\xi = \arg(\kappa_1) \approx .43\pi$. Using these values in our above analysis we find that with a sixth-order filter, $d = 3$, and $a_f = 1/4^d$, the mode is stabilized for $\sigma = 1$ since

$$\mathcal{A}_f = \mathcal{T}_f(\xi) e^{(s_r h) \sigma} \approx (1 - .06) (1 + .0176) \approx 0.96 \leq 1. \quad (54)$$

Of course this analysis does not rigourously apply to the full overlapping grid problem but it does give an indication of the expected behaviour.

6.2. Stability of the first-order wave equation

Consider the solution to the scalar first-order wave equation

$$u_t = u_x. \quad (55)$$

We discretize this equation in space using a centered difference approximation on the one-dimensional overlapping grid of Fig. 3 giving

$$\frac{\partial u_j^{(1)}}{\partial t} = \frac{u_{j+1}^{(1)} - u_{j-1}^{(1)}}{2h_1}, \quad j = 1, 2, 3, \dots, N-1 \quad (56)$$

$$\frac{\partial u_j^{(2)}}{\partial t} = \frac{u_{j+1}^{(2)} - u_{j-1}^{(2)}}{2h_2}, \quad j = q-1, q-2 \quad (57)$$

$$u_j^{(1)} = u_0(x_j^{(1)}), \quad j = 0, 1, 2, 3, \dots, N, \quad (58)$$

$$u_j^{(2)} = u_0(x_j^{(1)}), \quad j = q, q-1, q-2, \dots, \quad (59)$$

$$u_N^{(1)} = g(t), \quad (60)$$

$$u_0^{(1)} = \sum_{k=0}^r a_k u_k^{(2)}, \quad u_q^{(2)} = \sum_{k=0}^r b_k u_{p+k}^{(1)}. \quad (61)$$

Proceeding as in the previous section, we are led to study the eigenvalue problem for the semi-discrete, Laplace transformed solution,

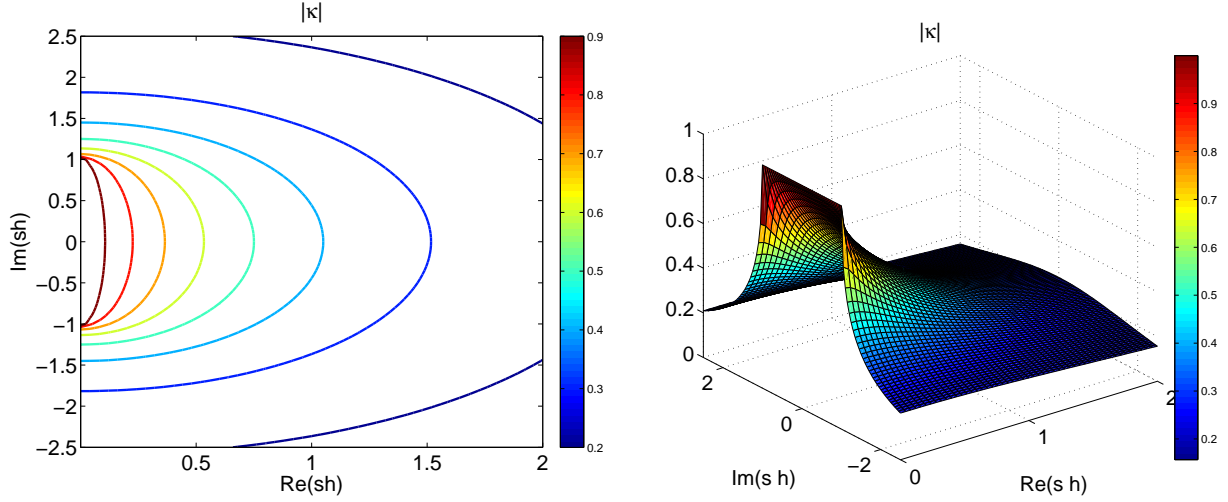


Fig. 7. Contours and surface plot of $|\kappa|$ from the first-order wave equation for the root $\kappa(sh)$ with $|\kappa| \leq 1$ for $Re(s) > 0$. The modulus of κ is one along the imaginary axis for $Im(sh) \in [-1, 1]$ and decays to zero as $Re(sh) \rightarrow \infty$.

$$2(sh_1)\tilde{u}_j^{(1)} = \tilde{u}_{j+1}^{(1)} - \tilde{u}_{j-1}^{(1)}, \quad j = 1, 2, 3, \dots, N-1, \quad (62)$$

$$2(sh_2)\tilde{u}_j^{(2)} = \tilde{u}_{j+1}^{(2)} - \tilde{u}_{j-1}^{(2)}, \quad j = q-1, q-2, \dots, \quad (63)$$

$$\tilde{u}_N^{(1)} = 0, \quad |\tilde{u}_j^{(2)}| < \infty, \quad (64)$$

$$\tilde{u}_0^{(1)} = \sum_{k=0}^r a_k \tilde{u}_k^{(2)}, \quad \tilde{u}_q^{(2)} = \sum_{k=0}^r b_k \tilde{u}_{p+k}^{(1)}. \quad (65)$$

The solution to this eigenvalue problem is

$$\tilde{u}_j^{(1)} = A(\kappa_1^j - (-1)^N (-\kappa_1)^{2N-j}), \quad j = 0, 1, 2, \dots, N \quad (66)$$

$$\tilde{u}_j^{(2)} = B(-\kappa_2)^{q-j}, \quad j = q, q-1, q-2, \dots, \quad (67)$$

where $\kappa_m(sh_m)$, $m = 1, 2$, are roots of the characteristic equation $\kappa^2 - 2(sh_m)\kappa - 1 = 0$ with $|\kappa_m(sh_m)| \leq 1$ for $Re(s) > 0$ and are given by

$$\begin{aligned} \kappa_m &= sh_m - \sqrt{(sh_m)^2 + 1}, \\ -\pi/2 &\leq \arg(\sqrt{(sh_m)^2 + 1}) < \pi/2. \end{aligned} \quad (68)$$

Fig. 7 shows $|\kappa|$ as a function of sh .

The solution (66)-(67) is of a similar form as that for the second-order wave equation and we are thus led to the following determinant condition for non-trivial solutions

$$G_f(s) = 1 - (-1)^N \kappa_1^{2N} - \left(\sum_{k=0}^r a_k (-\kappa_2)^{q-k} \right) \left(\sum_{k=0}^r b_k \left(\kappa_1^{p+k} - (-1)^N (-\kappa_1)^{2N-p-k} \right) \right). \quad (69)$$

The necessary Godunov-Ryabenkii condition for stability of solutions to equations (56)-(61) is that there be no roots of $G_f(s)$ with $Re(s) > 0$. The analogues of lemmas 1 and 2 hold true for the first-order wave equation,

Lemma 3 *If there is a solution to the eigenvalue problem (62)-(65) for given values $(s, h_1, h_2, \alpha, \beta, N)$, then for any $\gamma > 0$ there will be another solution (on a different grid) with values $(s\gamma, h_1/\gamma, h_2/\gamma, \alpha, \beta, N)$.*

Proof. The proof follows that of lemma 1 \square .

Lemma 4 *The growth-rate of solutions to the eigenvalue problem (62)-(65) with $G_f(s) = 0$, are bounded by $e^{(\gamma/h)t}$ where $\gamma = \gamma(r) \geq 0$ is a bounded constant that only depends on r .*

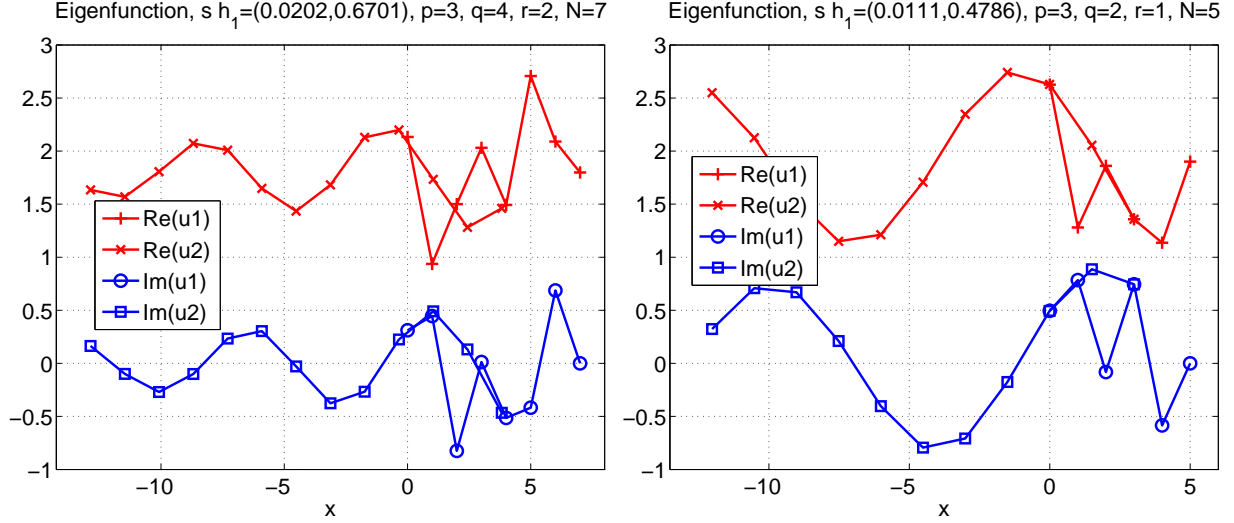


Fig. 8. First-order wave equation. Left: Overlapping grid eigenfunction for the unstable mode $s \approx (0.0202, 0.6701)$, $N = 7$ on the semi-infinite interval with quadratic interpolation. Right: Unstable mode for linear interpolation, $s \approx (0.01108, 0.4786)$.

Proof. The proof follows that of lemma 2 since $\kappa_m \rightarrow 0$ as $Re(s) \rightarrow \infty$ \square .

Olsson and Petersson [19] considered the infinite interval case and linear interpolation. The infinite interval case is obtained by setting the two terms $\kappa_1^{2N} = 0$ and $(-\kappa_1)^{2N-2p-k} = 0$ in the expression for $G_f(s)$. They showed that there are no eigenvalues with $Re(s) > 0$ but that there are generalized eigenvalues with $Re(s) = 0$ in the special case that $\alpha = 0$ and $\beta = 0$. These generalized eigenvalues will occur for any order of interpolation since the interpolation is always exact for $\alpha = \beta = 0$. For the finite interval case they found roots with $Re(s) > 0$. As the mesh was refined (increasing N) the real part of some of these roots increased proportional to $1/h^\gamma$ where $\gamma \approx .065$ and $\gamma \approx .033$ for the two cases presented. They also found roots whose real part decreased as the mesh was refined.

For the semi-infinite interval problem with linear or quadratic interpolation we can find roots with $Re(s) > 0$. We know analytically that these roots grow like $1/h$ as the mesh is refined when N is kept fixed. The evidence thus suggests that the case of keeping a fixed number of points, N , in the grid next to the boundary is the more difficult case compared to the situation when N is increased as the mesh is refined.

6.2.1. Examples of unstable modes for the first-order wave equation

We present two examples of unstable modes for the first-order wave equation that are determined as roots, $G_f(s) = 0$, of equation 69. For quadratic interpolation we use the overlap parameters

$$(h_1 = 1, h_2 \approx 1.3900, x_q^{(2)} - x_0^{(1)} = 3.8225, p = 3, q = 4, \alpha \approx 1.2500, \beta \approx 0.82250, N = 7)$$

and we numerically find the root of $G_f(s) = 0$ to be $sh_1 \approx (0.02022, 0.6701)$. For linear interpolation we use the grid parameters

$$(h_1 = 1, h_2 \approx 1.5025, x_q^{(2)} - x_0^{(1)} = 3.0000, p = 2, q = 3, \alpha \approx 0.0033278, \beta = 0.0, N = 5)$$

and we numerically find the root of $G_f(s) = 0$ to be $sh_1 \approx (0.01108, 0.4786)$. As for the second-order wave equation, these results were confirmed by computing all the eigenvalues of the matrix that results from the finite domain problem. The real and imaginary parts of the eigenfunctions for these two cases are shown in Fig. 8. We again note the poor agreement of the eigenfunctions in the overlap region.

6.2.2. Dissipation in the Godunov method

The Godonov method described in section 4.2 can be applied to the solution of the first order scalar wave equation, $u_t + cu_x = 0$ with $c > 0$. The second-order unlimited scheme (using $\mathcal{L}(b, c) = (b + c)/2$) is given by

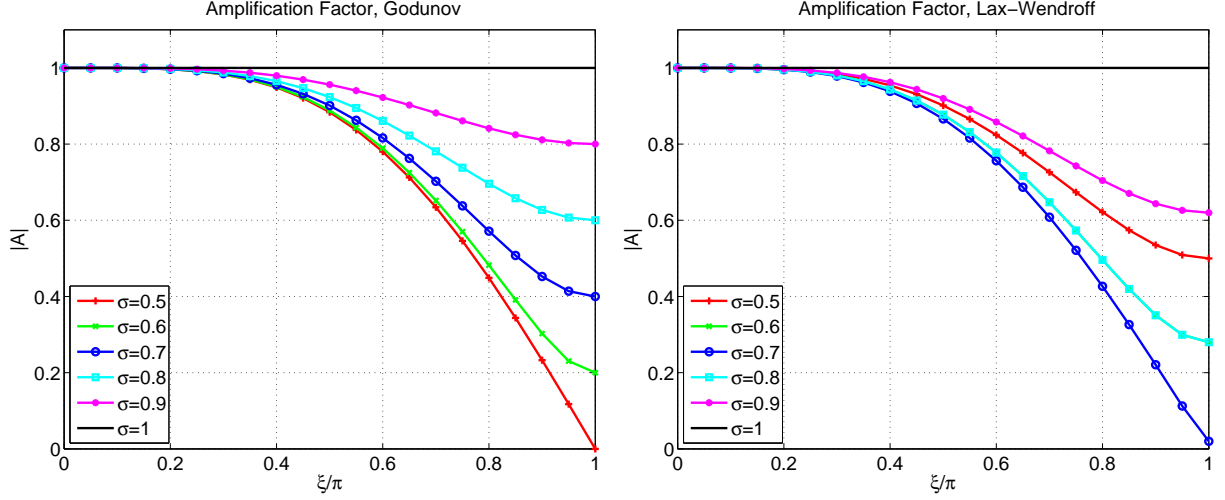


Fig. 9. The magnitude of the amplification factor for the Godunov scheme, $|\mathcal{A}_g|$, and the Lax-Wendroff scheme, $|\mathcal{A}_{lw}|$, for the one-dimensional first-order wave equation on a periodic domain. Note that $|\mathcal{A}_g(\sigma)| = |\mathcal{A}_g(1 - \sigma)|$ so that the curve for $\sigma = 0.3$ for the Godunov scheme is the same as the curve for $\sigma = 0.8$.

$$u_i^{n+1} = u_i^n - \sigma \Delta_0 u_i^n + \frac{\sigma^2}{2} \Delta_+ \Delta_- u_i^n + \frac{\sigma}{4} (1 - \sigma) \Delta_0 \Delta_+ u_i^n - \frac{\sigma}{8} (1 - \sigma) (\Delta_+ \Delta_-)^2 u_i^n, \quad (70)$$

where $\sigma = c\Delta t/dx$ is the CFL parameter. The first three terms on the right-hand side of (70) comprise the Lax-Wendroff scheme. The amplification factor, \mathcal{A}_g for the second-order un-limited Godunov scheme is obtained by substituting $u_i^n = \mathcal{A}_g^n e^{ij\xi}$ into (70) resulting in

$$\mathcal{A}_g(\xi, \sigma) = 1 - 2\sigma^2 \sin^2(\xi/2) - 2\sigma(1 - \sigma) \sin^4(\xi/2) - i\sigma \sin(\xi)(1 + (1 - \sigma) \sin^2(\xi/2)) \quad (71)$$

where $|\xi| \leq \pi$. Whence,

$$|\mathcal{A}_g(\xi, \sigma)|^2 = 1 - 2\sigma(1 - \sigma)(1 + \sigma^2 + (1 - \sigma)^2) \sin^4(\xi/2) - 4\sigma^2(1 - \sigma)^2 \sin^6(\xi/2). \quad (72)$$

Note that $|\mathcal{A}_g(\sigma)| = |\mathcal{A}_g(1 - \sigma)|$. For the Lax-Wendroff scheme, by comparison, we have

$$|\mathcal{A}_{lw}(\xi, \sigma)|^2 = 1 - 4\sigma^2(1 - \sigma^2) \sin^4(\xi/2). \quad (73)$$

Fig. 9 shows the magnitude of the amplification factor for a few selected values of σ . The magnitude of the amplification factor is of the same nature as the *transfer function* used to define the high-order filter (16) and shown in Fig. 2. The value $\sigma = \frac{1}{2}$ results in the most dissipation of high wave numbers for the Godunov scheme while the dissipation goes to zero when $\sigma = 1$ and $\sigma = 0$.

7. Adaptive Mesh Refinement

In this section we discuss the application of the adaptive mesh refinement (AMR) approach for solving the equations of elasticity on overlapping grids. AMR is a technique that adds fine grid patches to regions of the computational domain where more resolution is needed. AMR can dramatically speed up a computation and/or enable simulations with a much higher effective resolution compared to uniformly refining the grid. Block structured adaptive mesh refinement for hyperbolic problems was considered as early as 1973 by Browning, Kreiss and Olinger [13]. The AMR approach was further developed by Berger and Olinger [20] and later extended for shock hydrodynamics by Berger and Colella [21]. In previous work we have developed AMR algorithms for overlapping grids and have applied them to the solution of two-dimensional high-speed reactive flow problems with moving rigid bodies [22] and for parallel three-dimensional computations of reactive flows [2].

The adaptive mesh refinement (AMR) approach is designed to locally increase the grid resolution where an estimate of the error is large. This is done by adding refined grid patches to the existing base-level

component grids. The refinement grids are aligned with the underlying base grid (i.e. the refinement is done in parameter space) and are arranged in a hierarchy with the base grids belonging to level $\ell = 0$, the next finer grids being added to level $\ell = 1$ and so on. Grids on level ℓ are refined by a refinement ratio n_r from the grids on level $\ell - 1$. The grids are properly nested so that a grid on level ℓ is completely contained in the set of grids on the coarser level $\ell - 1$. This requirement is relaxed at physical boundaries to allow refinement grids to align with the boundary.

For simplicity, the numerical solution on all grids is advanced in time using the same time step. After every n_{regrid} time steps, the whole refined-grid hierarchy is rebuilt to accommodate the evolution of sharp features of the solution. This is done by first re-computing an estimate of the error given by

$$e_{\mathbf{i}} = \sum_{k=1}^{n_c} e_{k,\mathbf{i}}, \quad (74)$$

where the error is estimated as a sum of error estimates for each component,

$$e_{k,\mathbf{i}} = \frac{1}{3} \sum_{\alpha=1}^3 \left(\frac{c_1}{s_k} |\Delta_{0\alpha} u_{k,\mathbf{i}}| + \frac{c_2}{s_k} |\Delta_{+\alpha} \Delta_{-\alpha} u_{k,\mathbf{i}}| \right). \quad (75)$$

In (75), $\Delta_{0\alpha}$, $\Delta_{+\alpha}$ and $\Delta_{-\alpha}$ are the centered, forward and backward undivided difference operators in the α index direction, respectively, $u_{k,\mathbf{i}}$ is the k th component of the numerical solution for \mathbf{u} at grid index \mathbf{i} , s_k is a scale factor for component k , and c_1 and c_2 are weights. The error estimate used here follows that introduced in [22] for compressible flows where it was found to be an effective choice, although other methods are possible. Once the error estimate is computed, it is smoothed and then grid points are tagged for refinement where $e_{\mathbf{i}}$ is greater than a chosen tolerance. Buffer points are added to increase the region of tagged points slightly (so that fewer regrids are needed), and a new overlapping grid hierarchy is build to cover the buffered region of tagged points. (Typically, the width of the buffer is taken to be 2 so that $n_{\text{regrid}} = 2n_r$, see [22].) The numerical solution is then transferred from the old grid hierarchy to the new one, and the time-stepping proceeds for the solution on the new grid hierarchy until the next gridding step. Note that the SOS-C scheme uses three time levels and thus at each regrid step we transfer (interpolate) the solutions at the two times t and $t - \Delta t$ from the old grid hierarchy to the new.

The accuracy of the AMR approach is verified in Section 8.4 for a traveling pulse. In Section 8.7 AMR is used to compute the diffraction of p-wave by a cylindrical cavity.

8. Numerical results

In this section we present numerical results to verify the correctness of the implementations and the accuracy and stability of the approximations. We compare results from the SOS-C and FOS-G approximations. We begin by computing solutions and errors with the method of analytic solutions, a powerful technique for generating synthetic exact solutions for testing numerical approximations. We then determine the errors when computing known solutions to a two-dimensional problem in an annular domain and a three dimensional problem in a spherical domain. In section 8.8 we provide some CPU timing results. We conclude this section by presenting results from an interesting problem with complex geometry.

8.1. The method of analytic solutions

The *method of analytic solutions* is a very useful technique for constructing exact solutions to check the accuracy of a numerical implementation. This method, also sometimes known as the *method of manufactured solutions* [23], or *twilight-zone forcing* [1] adds forcing functions to the governing equations and boundary conditions. These forcing functions are determined so that some given functions, $\bar{u}(\mathbf{x}, t)$, will be the exact solution to the forced equations. With this approach, the error in the discrete solution can be easily determined. To illustrate the technique, consider solving the IBVP for the equations of linear elasticity in second-order form,

$$\begin{aligned}
\rho \mathbf{u}_{tt} &= (\lambda + \mu) \nabla(\nabla \cdot \mathbf{u}) + \mu \Delta \mathbf{u} + \mathbf{f}, & \text{for } \mathbf{x} \in \Omega, \\
\mathbf{u}(x, 0) &= \mathbf{u}_0(\mathbf{x}), \quad \mathbf{u}_t(x, 0) = \mathbf{u}_1(\mathbf{x}), & \text{for } \mathbf{x} \in \Omega, \text{ at } t = 0, \\
\mathbf{u}(\mathbf{x}, t) &= \mathbf{g}(\mathbf{x}, t), & \text{for } \mathbf{x} \in \partial\Omega.
\end{aligned}$$

Any given smooth function, $\bar{\mathbf{u}}(\mathbf{x}, t)$, will be an exact solution of the IBVP if we set the forcing function, initial conditions and boundary conditions as

$$\begin{aligned}
\mathbf{f}(\mathbf{x}, t) &= \rho \bar{\mathbf{u}}_{tt} - (\lambda + \mu) \nabla(\nabla \cdot \bar{\mathbf{u}}) - \mu \Delta \bar{\mathbf{u}}, \\
\mathbf{u}_0(\mathbf{x}) &= \bar{\mathbf{u}}(\mathbf{x}, 0), \quad \mathbf{u}_1(\mathbf{x}) = \bar{\mathbf{u}}_t(\mathbf{x}, 0), \quad \text{and} \quad \mathbf{g}(\mathbf{x}, t) = \bar{\mathbf{u}}(\mathbf{x}, t).
\end{aligned}$$

In our numerical implementation, we have a number of choices available for $\bar{\mathbf{u}}$, including polynomials, trigonometric functions, and exponential functions, among others.

Low order polynomial solutions can be used to check that the approximations are exact on Cartesian grids. For most of the results in the following sections we use a trigonometric exact solution. In two dimensions the trigonometric solution is

$$\begin{aligned}
\bar{u}_1 &= (1/2) \cos(\pi f_x x) \cos(\pi f_y y) \cos(\pi f_t t), \\
\bar{u}_2 &= (1/2) \sin(\pi f_x x) \cos(\pi f_y y) \cos(\pi f_t t), \\
\bar{v}_1 &= (3/4) \sin(\pi f_x x) \cos(\pi f_y y) \cos(\pi f_t t), \\
\bar{v}_2 &= (1/4) \sin(\pi f_x x) \sin(\pi f_y y) \cos(\pi f_t t), \\
\bar{\sigma}_{11} &= -(1/2) \cos(\pi f_x x) \cos(\pi f_y y) \cos(\pi f_t t), \\
\bar{\sigma}_{12} &= (2/5) \sin(\pi f_x x) \cos(\pi f_y y) \cos(\pi f_t t), \\
\bar{\sigma}_{21} &= (2/5) \sin(\pi f_x x) \cos(\pi f_y y) \cos(\pi f_t t), \\
\bar{\sigma}_{22} &= (3/5) \cos(\pi f_x x) \sin(\pi f_y y) \cos(\pi f_t t),
\end{aligned} \tag{76}$$

while in three dimensions we use

$$\begin{aligned}
\bar{u}_1 &= \cos(\pi f_x x) \cos(\pi f_y y) \cos(\pi f_z z) \cos(\pi f_t t), \\
\bar{u}_2 &= (1/2) \cos(\pi f_x x) \sin(\pi f_y y) \cos(\pi f_z z) \cos(\pi f_t t), \\
\bar{u}_3 &= (3/4) \cos(\pi f_x x) \cos(\pi f_y y) \sin(\pi f_z z) \cos(\pi f_t t), \\
\bar{v}_1 &= (3/4) \sin(\pi f_x x) \cos(\pi f_y y) \cos(\pi f_z z) \cos(\pi f_t t), \\
\bar{v}_2 &= (1/4) \cos(\pi f_x x) \cos(\pi f_y y) \sin(\pi f_z z) \cos(\pi f_t t), \\
\bar{v}_3 &= -(1/2) \sin(\pi f_x x) \sin(\pi f_y y) \sin(\pi f_z z) \cos(\pi f_t t), \\
\bar{\sigma}_{11} &= -(1/2) \cos(\pi f_x x) \cos(\pi f_y y) \cos(\pi f_z z) \cos(\pi f_t t), \\
\bar{\sigma}_{12} &= (2/5) \sin(\pi f_x x) \cos(\pi f_y y) \cos(\pi f_z z) \cos(\pi f_t t), \\
\bar{\sigma}_{13} &= (3/5) \cos(\pi f_x x) \cos(\pi f_y y) \sin(\pi f_z z) \cos(\pi f_t t), \\
\bar{\sigma}_{21} &= (2/5) \sin(\pi f_x x) \cos(\pi f_y y) \cos(\pi f_z z) \cos(\pi f_t t), \\
\bar{\sigma}_{22} &= -(7/10) \sin(\pi f_x x) \cos(\pi f_y y) \sin(\pi f_z z) \cos(\pi f_t t), \\
\bar{\sigma}_{23} &= (.65) \cos(\pi f_x x) \sin(\pi f_y y) \sin(\pi f_z z) \cos(\pi f_t t), \\
\bar{\sigma}_{31} &= (3/5) \cos(\pi f_x x) \cos(\pi f_y y) \sin(\pi f_z z) \cos(\pi f_t t), \\
\bar{\sigma}_{32} &= (.65) \cos(\pi f_x x) \sin(\pi f_y y) \sin(\pi f_z z) \cos(\pi f_t t), \\
\bar{\sigma}_{33} &= -(1/5) \sin(\pi f_x x) \sin(\pi f_y y) \sin(\pi f_z z) \cos(\pi f_t t).
\end{aligned} \tag{77}$$

The second-order-system only requires \bar{u}_m . The first-order-system also uses \bar{v}_m and $\bar{\sigma}_{mn}$. Note that \bar{u}_m , \bar{v}_m and $\bar{\sigma}_{mn}$ are chosen as independent functions and thus, for example, \bar{v}_m is not the time derivative of \bar{u}_m .

8.2. Circular void in a square

We solve the equations of elasticity in the two-dimensional domain Ω_{CV} that consists on a square region with a circular hole as shown in Fig. 10. We use the method of analytic solutions as described in Section 8.1 with the trigonometric polynomial solution (76) with $f_x = f_y = f_t = 1$. We solve the elasticity equations on a

sequence of grids with increasing resolution and determine the maximum errors and estimated convergence rate. To be specific, the domain is defined as $\Omega_{CV} = [-1, 1]^2 - \Omega_D$, where Ω_D is the circular disk of radius $R = .5$. The grid for an annular region is defined by

$$\mathcal{A}([r_a, r_b], N_1, N_2) = \left\{ (r_{i_2} \cos(\theta_{i_1}), r_{i_2} \sin(\theta_{i_1})) \mid \theta_{i_1} = 2\pi i_1 / N_1, r_{i_2} = r_a + (r_b - r_a) i_2 / N_2, \right. \\ \left. i_k = 0, 1, \dots, N_k, k = 1, 2 \right\}.$$

The grid for a rectangle is

$$\mathcal{R}([x_a, x_b] \times [y_a, y_b], N_1, N_2) = \left\{ (x_a + (x_b - x_a) i_1 / N_1, y_a + (y_b - y_a) i_2 / N_2) \mid i_k = 0, 1, \dots, N_k, k = 1, 2 \right\}.$$

The number of grid points in each coordinate direction for a grid with resolution factor j is chosen so that the grid spacing is approximately

$$\Delta s^{(j)} = \frac{1}{10j}.$$

The composite grid for Ω_{CV} is composed of a background square and an annular grid,

$$\mathcal{G}_{CV}^{(j)} = \mathcal{R}([-1, 1]^2, N_x(j), N_x(j)) \cup \mathcal{A}([R, R + .25], N_\theta(j), N_r(j)),$$

where $N_x(j) = \lfloor 2/\Delta s^{(j)} + 1.5 \rfloor$, $N_\theta(j) = \lfloor 2\pi(R + .125)/\Delta s^{(j)} + 1.5 \rfloor$ and $N_r(j) = \lfloor .25/\Delta s^{(j)} + 2.5 \rfloor$. Here $\lfloor x \rfloor$ denotes the largest integer less than or equal to x .

Figures 11 and 12 contain the maximum errors and convergence rates for the displacement and traction boundary conditions, respectively. Columns titled “r” in the figures contain the ratio of the error from the current resolution to the previous. These ratios should be approximately equal to four for a second-order accurate scheme. The errors are shown graphically in Fig. 13. These results are for $\lambda = 1$ and $\mu = 1$. The convergence rates are all reasonably close to two. Fig. 10 shows the grid $\mathcal{G}_{CV}^{(2)}$, along with a component of the solution and error for this problem.

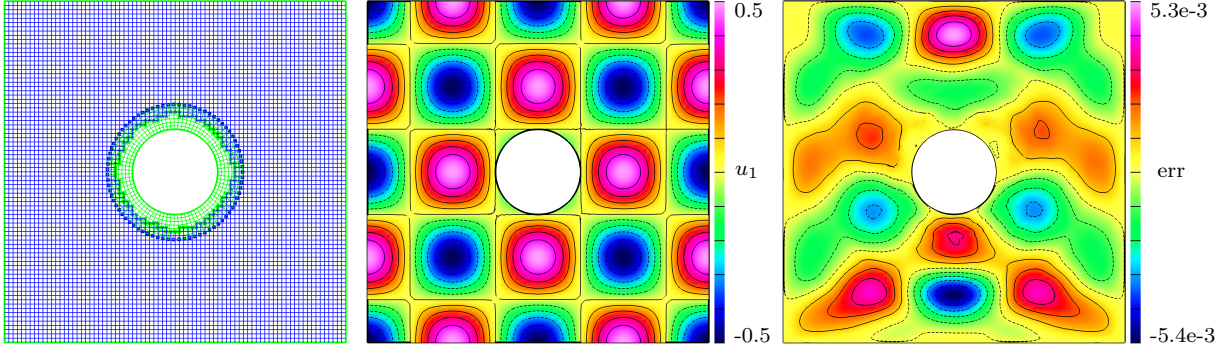


Fig. 10. Circular void in a square with a trigonometric analytic solution: grid $\mathcal{G}_{CV}^{(2)}$, solution u_1 , and error in u_1 at $t = 1$ (SOS-C).

8.3. Spherical void in a box

In this example we consider a geometry consisting of a spherical void in a box as shown in Figure 14. We solve the three-dimensional elasticity equations using the method of analytic solutions with the trigonometric solution (77) and $f_x = f_y = f_z = f_t = 0.5$. The composite grid for this geometry is shown in Figure 14 and consists of a Cartesian background grid and two orthographic patches that cover the sphere. The box grid is defined as

$$\mathcal{B}([x_a, x_b] \times [y_a, y_b] \times [z_a, z_b], N_1, N_2, N_3) = \left\{ (x_a + i_1 \Delta x, y_a + i_2 \Delta y, z_a + i_3 \Delta z) \mid \right. \\ \left. \Delta x = (x_b - x_a)/N_1, \Delta y = (y_b - y_a)/N_2, \Delta z = (z_b - z_a)/N_3, i_\alpha = 0, 1, \dots, N_\alpha, \alpha = 1, 2, 3 \right\}. \quad (78)$$

			SOS-C		FOS-G					
Grid	$\mathcal{G}_{CV}^{(j)}$	$\Delta s^{(j)}$	$e_u^{(j)}$	r	$e_u^{(j)}$	r	$e_v^{(j)}$	r	$e_\sigma^{(j)}$	r
	$\mathcal{G}_{CV}^{(1)}$	1/10	1.2×10^{-2}		2.8×10^{-3}		5.8×10^{-3}		2.1×10^{-2}	
	$\mathcal{G}_{CV}^{(2)}$	1/20	3.1×10^{-3}	4.0	5.6×10^{-4}	5.0	1.6×10^{-3}	3.6	5.8×10^{-3}	3.7
	$\mathcal{G}_{CV}^{(4)}$	1/40	7.8×10^{-4}	4.0	1.3×10^{-4}	4.2	4.2×10^{-4}	3.9	1.5×10^{-3}	3.9
	$\mathcal{G}_{CV}^{(8)}$	1/80	1.9×10^{-4}	4.0	3.5×10^{-5}	3.8	1.1×10^{-4}	3.8	3.8×10^{-4}	3.9
rate			2.00		2.10		1.91		1.94	

Fig. 11. Circular void in a square with a trigonometric analytic solution: maximum errors and convergence rates at $t = 0.5$ for displacement boundary conditions. The columns labeled “r” contain the ratio of the error at the current resolution to that at the previous resolution.

			SOS-C		FOS-G					
Grid	$\mathcal{G}_{CV}^{(j)}$	$\Delta s^{(j)}$	$e_u^{(j)}$	r	$e_u^{(j)}$	r	$e_v^{(j)}$	r	$e_\sigma^{(j)}$	r
	$\mathcal{G}_{CV}^{(1)}$	1/10	2.1×10^{-2}		5.2×10^{-3}		1.3×10^{-2}		3.7×10^{-2}	
	$\mathcal{G}_{CV}^{(2)}$	1/20	5.7×10^{-3}	3.6	1.0×10^{-3}	5.2	2.3×10^{-3}	5.9	6.9×10^{-3}	5.4
	$\mathcal{G}_{CV}^{(4)}$	1/40	1.6×10^{-3}	3.6	2.1×10^{-4}	4.8	4.6×10^{-4}	4.9	1.4×10^{-3}	4.9
	$\mathcal{G}_{CV}^{(8)}$	1/80	4.2×10^{-4}	3.8	5.0×10^{-5}	4.2	1.2×10^{-4}	4.0	3.4×10^{-4}	4.2
rate			1.88		2.24		2.28		2.26	

Fig. 12. Circular void in a square with a trigonometric analytic solution: maximum errors and convergence rates at $t = 0.5$ for traction boundary conditions.

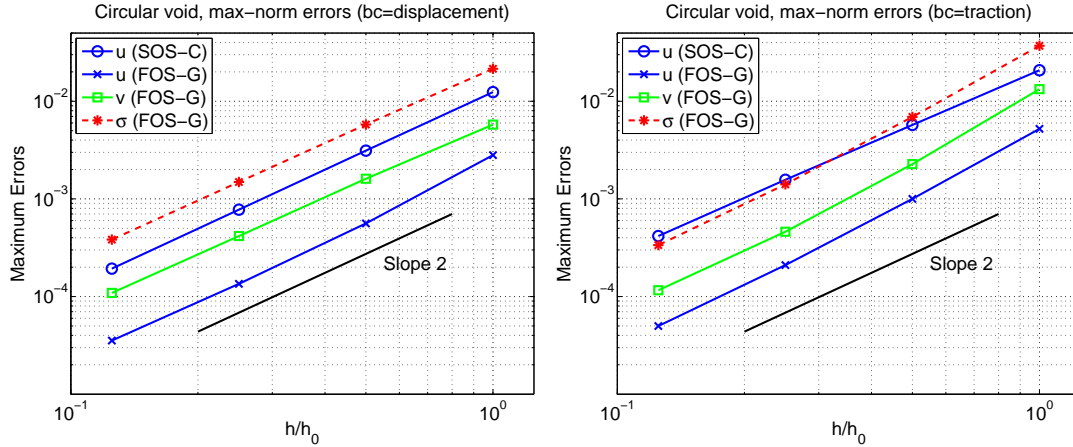


Fig. 13. Circular void in a square with a trigonometric analytic solution: maximum errors at $t = 0.5$ as a function of grid spacing. Left: displacement boundary conditions. Right: traction boundary conditions.

The grids on the sphere are defined in terms of the orthographic transform \mathbf{O}_p , given by

$$\mathbf{x} = \mathbf{O}_p(\mathbf{r}; [\rho_a, \rho_b], \hat{s}_2, \hat{s}_3) \equiv \left(p \frac{(1 - \sigma^2)\rho}{1 + \sigma^2}, \frac{2\rho s_2}{1 + \sigma^2}, p \frac{2\rho s_3}{1 + \sigma^2} \right),$$

where ρ , s_2 , s_3 and σ are given in terms of $\mathbf{r} = (r_1, r_2, r_3) \in [0, 1]^3$ by

$$\rho = \rho_a + r_1(\rho_b - \rho_a), \quad s_2 = \left(r_2 - \frac{1}{2} \right) \hat{s}_2, \quad s_3 = \left(r_3 - \frac{1}{2} \right) \hat{s}_3, \quad \sigma^2 = s_2^2 + s_3^2,$$

and $p = +1$ for the transformation near the north pole and $p = -1$ for the transformation near the south pole. The parameters $[\rho_a, \rho_b]$ specify the radial extent of the region, while \hat{s}_2 and \hat{s}_3 determine its lateral

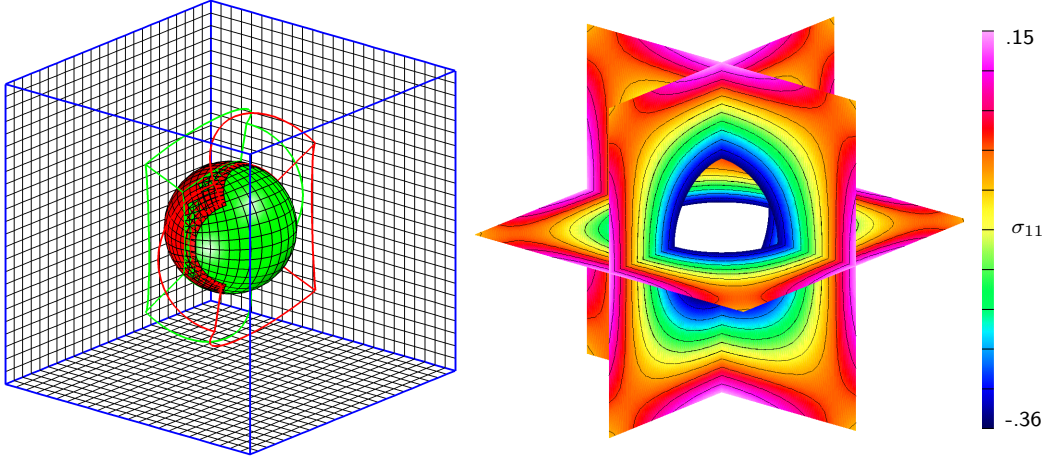


Fig. 14. Spherical void in a box with a trigonometric analytic solution: grid $\mathcal{G}_s^{(2)}$ and solution σ_{11} at $t = 0.1$ (FOS-G).

extent. The orthographic grid, \mathcal{O}_p centered about pole p , is now defined as

$$\mathcal{O}_p([\rho_a, \rho_b], \hat{s}_2, \hat{s}_3, N_1, N_2, N_3) = \{\mathbf{x}_i \mid \mathbf{x}_i = \mathbf{O}_p(\mathbf{r}_i; [\rho_a, \rho_b], \hat{s}_2, \hat{s}_3), i_\alpha = 0, 1, \dots, N_\alpha, \alpha = 1, 2, 3\}. \quad (79)$$

The number of grid points in each coordinate direction for a grid with resolution factor j is chosen so that the grid spacing is approximately $\Delta s^{(j)} = 1/(5j)$. The sphere-in-a-box composite grid is then defined as

$$\mathcal{G}_s^{(j)} = \mathcal{B}([-1.2, 1.2]^3, N_x(j), N_x(j), N_x(j)) \cup \mathcal{O}_{\pm 1}([.5, .9], 2.1, 2.1, N_r(j), N_o(j), N_o(j)),$$

where $N_x(j) = \lfloor 2.4/\Delta s^{(j)} + 1.5 \rfloor$, $N_r(j) = \lfloor 0.4/\Delta s^{(j)} + 1.5 \rfloor$ and $N_o(j) = \lfloor 2.24/\Delta s^{(j)} + 1.5 \rfloor$.

Results for this composite grid using the trigonometric exact solution (77) and displacement boundary conditions are given in Fig 15 while results for traction boundary conditions are given in Fig 16. The finest grid used, $\mathcal{G}_s^{(8)}$ had about 1 million grid points. The convergence rates for the SOS-C and FOS-G schemes are reasonably close to 2. Some of the variables for FOS-G seem to be converging at a rate larger than 2 but this likely caused by the grids being still relatively coarse.

			SOS-C		FOS-G					
Grid	$\mathcal{G}_s^{(j)}$	$\Delta s^{(j)}$	$e_u^{(j)}$	r	$e_u^{(j)}$	r	$e_v^{(j)}$	r	$e_\sigma^{(j)}$	r
	$\mathcal{G}_s^{(2)}$	1/10	7.1×10^{-3}		1.5×10^{-3}		2.9×10^{-3}		1.5×10^{-2}	
	$\mathcal{G}_s^{(4)}$	1/20	6.6×10^{-4}	10.7	2.5×10^{-4}	6.0	4.3×10^{-4}	6.7	3.7×10^{-3}	4.1
	$\mathcal{G}_s^{(8)}$	1/40	1.4×10^{-4}	4.7	3.6×10^{-5}	7.0	1.0×10^{-4}	4.2	9.1×10^{-4}	4.0
rate			2.82		2.70		2.41		2.02	

Fig. 15. Spherical void in a box with a trigonometric analytic solution: maximum errors and convergence rates at $t = 0.1$ for displacement boundary conditions. The columns labeled “r” contain the ratio of the error at the current resolution to that at the previous resolution.

8.4. Traveling pulse with AMR

In this section we verify the accuracy of the adaptive mesh refinement option described in Section 7. We compute the solution to a *pulse* that travels through an overlapping grid with an embedded rotated grid. The traveling pulse solution is defined with the method of analytic solutions described in section 8.1 and is given by

$$\bar{\mathbf{u}}(\mathbf{x}, t) = \mathbf{c}_0 \exp \left\{ -(|\mathbf{x} - \mathbf{x}_c(t)|/c_1)^2 \right\}, \quad (80)$$

where \mathbf{c}_0 and c_1 are parameters, and $\mathbf{x}_c(t) = \mathbf{x}_0 + \mathbf{v}_0 t$ gives the position of the center of the pulse at a time t . Here, \mathbf{x}_0 is the position of the center of the pulse at $t = 0$ and \mathbf{v}_0 is its constant velocity. The computations

			SOS-C		FOS-G					
Grid	$\mathcal{G}_s^{(j)}$	$\Delta s^{(j)}$	$e_u^{(j)}$	r	$e_u^{(j)}$	r	$e_v^{(j)}$	r	$e_\sigma^{(j)}$	r
	$\mathcal{G}_s^{(2)}$	1/10	8.3×10^{-3}		1.5×10^{-3}		7.8×10^{-3}		2.1×10^{-2}	
	$\mathcal{G}_s^{(4)}$	1/20	2.0×10^{-3}	4.2	2.5×10^{-4}	6.0	1.0×10^{-3}	7.6	5.2×10^{-3}	4.1
	$\mathcal{G}_s^{(8)}$	1/40	4.9×10^{-4}	4.0	3.6×10^{-5}	7.0	2.3×10^{-4}	4.4	1.3×10^{-3}	4.1
rate			2.04		2.70		2.53		2.03	

Fig. 16. Spherical void in a box with a trigonometric analytic solution: maximum errors and convergence rates at $t = 0.1$ for traction boundary conditions. The columns labeled “r” contain the ratio of the error at the current resolution to that at the previous resolution.

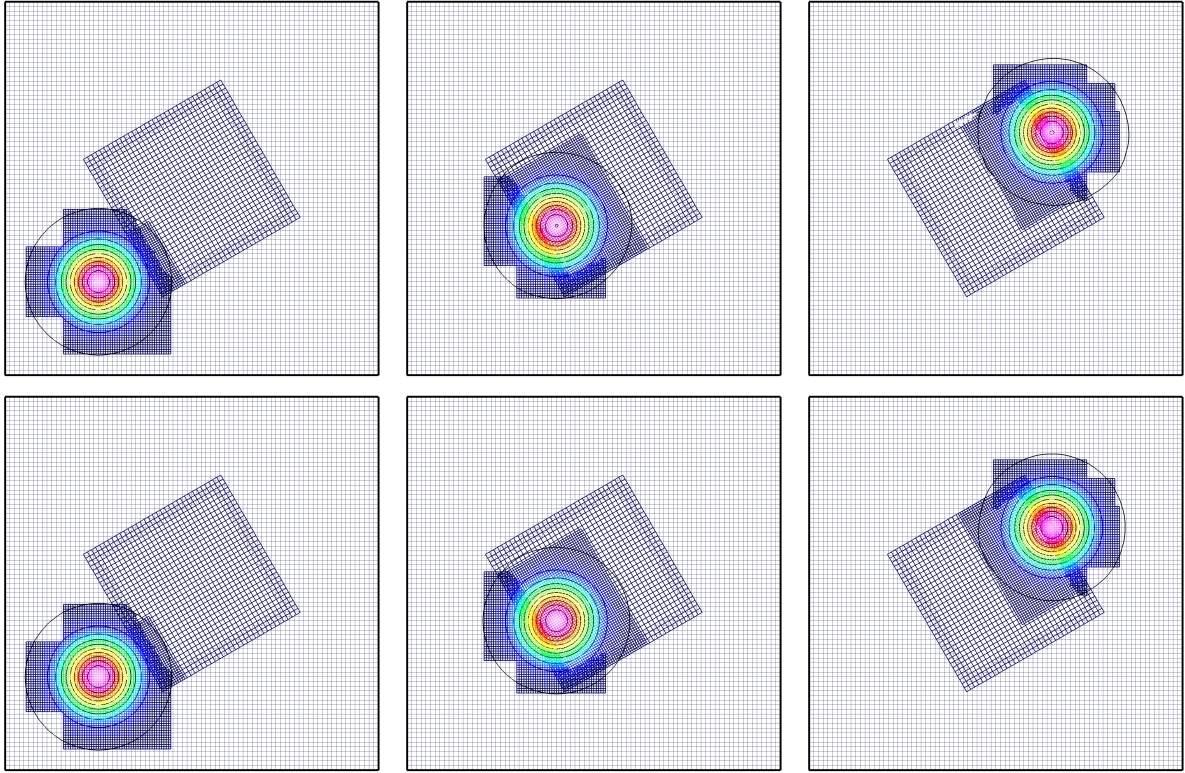


Fig. 17. Propagation of a pulse through an embedded rotated grid, computed using AMR. The locations of the refinement grids are recomputed every 4 time-steps. Contours of the displacement u_1 at times $t = 0$ (left), $t = 0.3$ (middle), and $t = 0.8$ (right), are plotted so that the grids are also shown. Top: results from SOS-C. Bottom: results from FOS-G.

used $\mathbf{x}_0 = (-0.5, -0.5)$, $\mathbf{v}_0 = (1, 1)$, $c_1 = 1/30$ and $\mathbf{c}_0 = \mathbf{1}$. There was one refinement level of refinement ratio $n_r = 2$.

The rotated-square-in-a-square grid, $\mathcal{G}_r^{(j)}$, for this case was defined as the union of a back-ground Cartesian grid for the square $[-1, 1]^2$ together with a Cartesian grid for the domain $[-0.4, 0.4]^2$ that is rotated by 45° about its center. The grid spacing for resolution factor j was $\Delta s^{(j)} \approx 1/10^j$. Figure 17 shows results of this computation for the SOS-C and FOS-G methods. The solution is seen to pass through the grid interfaces with little apparent distortion. The maximum errors and convergence rates for this problem are given in Fig. 18. The results indicate that the solution converges at second-order accuracy.

			SOS-C		FOS-G					
Grid	$\mathcal{G}_r^{(j)}$	$\Delta s^{(j)}$	$e_u^{(j)}$	r	$e_u^{(j)}$	r	$e_v^{(j)}$	r	$e_\sigma^{(j)}$	r
	$\mathcal{G}_r^{(1)}$	1/10	3.7×10^{-2}		5.6×10^{-3}		2.2×10^{-2}		4.3×10^{-2}	
	$\mathcal{G}_r^{(2)}$	1/20	6.1×10^{-3}	6.1	1.4×10^{-3}	3.8	5.3×10^{-3}	4.2	1.1×10^{-2}	3.9
	$\mathcal{G}_r^{(4)}$	1/40	1.5×10^{-3}	4.0	3.7×10^{-4}	3.9	1.4×10^{-3}	3.7	2.5×10^{-3}	4.3
	$\mathcal{G}_r^{(8)}$	1/80	3.9×10^{-4}	4.0	6.8×10^{-5}	5.4	3.6×10^{-4}	4.0	6.3×10^{-4}	4.0
rate			2.18		2.11		1.97		2.03	

Fig. 18. Traveling pulse with AMR on a rotated-square-in-a-square grid. The maximum errors and estimated convergence rates at $t = 1.0$ are given for the SOC-C and SOS-G methods.

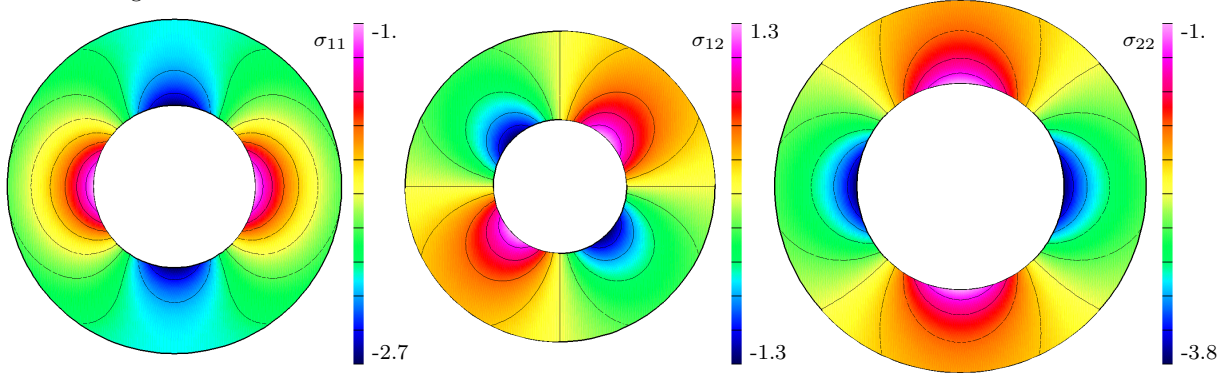


Fig. 19. Vibrational mode $n = 1$ of an elastic annulus with traction boundary conditions (case 2). Contours of different components of the stress at different times plotted on the deformed grid, scaling the displacement by a factor of 0.25. Left: σ_{11} at $t = 0$. Middle: σ_{12} at $t = 0.6$. Right: σ_{22} at $t = 2.0$.

8.5. Vibrational modes of an elastic annulus

Consider the two-dimensional annular domain with inner radius r_a and outer radius r_b , $\Omega_A = \{\mathbf{x} \in \mathbb{R}^2 \mid r_a \leq |\mathbf{x}| \leq r_b\}$. Solutions that only depend on the radius r and time t will satisfy the equation

$$\rho \frac{\partial^2}{\partial t^2} u_r = (\lambda + 2\mu) \frac{\partial}{\partial r} \left(\frac{1}{r} \frac{\partial}{\partial r} (r u_r) \right). \quad (81)$$

where $u_r = \cos(\theta)u_1 + \sin(\theta)u_2$ is the radial component of the displacement. We consider solutions satisfying displacement boundary conditions,

$$u_r(r, t) = 0, \quad \text{at } r = r_a, r_b, \quad (82)$$

or traction boundary conditions

$$\sigma_{rr}(r, t) = \lambda \frac{1}{r} \frac{\partial}{\partial r} (r u_r) + 2\mu \frac{\partial}{\partial r} u_r = 0, \quad \text{at } r = r_a, r_b. \quad (83)$$

The time independent solution to (81) is of the form

$$u_r = Ar + \frac{B}{r}.$$

For traction boundary conditions with a constant pressure p_a on the inner surface at $r = r_a$ and a constant pressure p_b on the outer surface at $r = r_b$ the solution is (see Love [24], page 144),

$$A = \frac{p_b r_b^2 - p_a r_a^2}{2(\lambda + \mu)(r_a^2 - r_b^2)}, \quad B = \frac{(p_b - p_a)r_a^2 r_b^2}{2\mu(r_a^2 - r_b^2)}. \quad (84)$$

The time harmonic solutions to (81), $u_r(r, t) = U(r) e^{-i\omega t}$, satisfy

$$U(r) = A_n J_1(\alpha_n r) + B_n Y_1(\alpha_n r),$$

where J_1 and Y_1 are the Bessel functions of the first and second kind, and $\alpha_n^2 = \omega_n^2 \rho / (\lambda + 2\mu)$, $n = 1, 2, 3, \dots$. For displacement boundary conditions, α_n are roots of the eigenvalue equation

$$\Lambda_D(\alpha) = J_1(\alpha r_a) Y_1(\alpha r_b) - J_1(\alpha r_b) Y_1(\alpha r_a) = 0.$$

while for traction boundary conditions α_n are roots of

$$\begin{aligned} \Lambda_T(\alpha) &= G_J(\alpha r_a) G_Y(\alpha r_b) - G_J(\alpha r_b) G_Y(\alpha r_a) = 0, \\ G_J(\alpha r) &= (\lambda + 2\mu) \alpha r J_1'(\alpha r) + \lambda J_1(\alpha r), \\ G_Y(\alpha r) &= (\lambda + 2\mu) \alpha r Y_1'(\alpha r) + \lambda Y_1(\alpha r). \end{aligned}$$

To evaluate the accuracy of the numerical schemes we are thus led to consider the exact solution

$$\bar{u}_r = Ar + \frac{B}{r} + (A_n J_1(\alpha_n r) + B_n Y_1(\alpha_n r)) \cos(\omega_n t). \quad (85)$$

We consider four cases with boundary conditions and parameters given in Fig. 20. For all cases we look at mode $n = 1$ and $r_b/r_a = 2$. The first two cases consider displacement and traction boundary conditions for $\lambda/\mu = 1$ while the latter two cases use $\lambda/\mu = 100$.

Case	BC	λ/μ	(p_a, p_b)	α_1	A_1	B_1
1	D	1	(0, 0)	6.3931567616	1.8502739846	-1.3135880300
2	T	1	(1, 2)	1.3113530190	0.1861924685	-0.1140163754
3	D	100	(1, 2)	6.3931567616	1.8502739846	-1.3135880300
4	T	100	(1, 2)	6.2525010635	1.7624191636	1.6031685352

Fig. 20. Parameters used in computing the vibrational modes of the annulus. The boundary condition, BC, is either displacement (D) or traction (T).

The composite grid for the annulus Ω_A is composed of a single annular grid of inner radius $\frac{1}{2}$ and outer radius 1,

$$\mathcal{G}_A^{(j)} = \mathcal{A}([\frac{1}{2}, 1], N_\theta, N_r),$$

where $N_r = \lfloor .5/\Delta s^{(j)} + 2.5 \rfloor$, $N_\theta = \lfloor 2\pi(.75)/\Delta s^{(j)} + 1.5 \rfloor$, and the grid spacing is $\Delta s^{(j)} = 1/(10j)$.

Fig. 23 and Figures 21-22 show the maximum errors on a sequence of grids and estimate convergence rates for the displacement and traction boundary conditions for $\lambda = \mu = 1$. The convergence rates are close to the expected value of 2. Figure 19 shows the solution at a few different times.

Results for $\lambda = 100$, $\mu = 1$ are given in figure 26. and Figures 24-25. This case is more difficult as many more time steps are required to reach the final time and the traction boundary conditions can be sensitive for large λ/μ . The FOS-G results for traction boundary conditions show convergence rates that are slightly larger than expected.

			SOS-C		FOS-G					
Grid	$\mathcal{G}^{(j)}$	$\Delta s^{(j)}$	$e_u^{(j)}$	r	$e_u^{(j)}$	r	$e_v^{(j)}$	r	$e_\sigma^{(j)}$	r
	$\mathcal{G}^{(1)}$	1/10	2.4×10^{-2}		5.9×10^{-3}		5.2×10^{-1}		3.0×10^{-1}	
	$\mathcal{G}^{(2)}$	1/20	7.2×10^{-3}	3.3	2.2×10^{-3}	2.6	1.1×10^{-1}	4.9	4.5×10^{-2}	6.7
	$\mathcal{G}^{(4)}$	1/40	1.9×10^{-3}	3.7	6.7×10^{-4}	3.3	2.2×10^{-2}	4.8	1.6×10^{-2}	2.7
	$\mathcal{G}^{(8)}$	1/80	4.9×10^{-4}	3.9	1.8×10^{-4}	3.7	4.3×10^{-3}	5.2	4.7×10^{-3}	3.5
	$\mathcal{G}^{(16)}$	1/160	1.3×10^{-4}	3.9	4.2×10^{-5}	4.2	9.0×10^{-4}	4.7	1.1×10^{-3}	4.1
rate			1.90		1.79		2.30		1.93	

Fig. 21. Vibrational modes of an annulus, case 1. Maximum errors and estimates convergence rates for displacement boundary conditions at $t = 0.5$ with $\lambda/\mu = 1$.

			SOS-C		FOS-G					
Grid	$\mathcal{G}^{(j)}$	$\Delta s^{(j)}$	$e_u^{(j)}$	r	$e_u^{(j)}$	r	$e_v^{(j)}$	r	$e_\sigma^{(j)}$	r
	$\mathcal{G}^{(1)}$	1/10	7.4×10^{-4}		6.5×10^{-3}		1.6×10^{-2}		4.3×10^{-2}	
	$\mathcal{G}^{(2)}$	1/20	1.8×10^{-4}	4.0	1.7×10^{-3}	3.9	4.2×10^{-3}	3.9	1.1×10^{-2}	3.9
	$\mathcal{G}^{(4)}$	1/40	6.1×10^{-5}	3.0	3.8×10^{-4}	4.5	9.8×10^{-4}	4.3	2.6×10^{-3}	4.4
	$\mathcal{G}^{(8)}$	1/80	1.8×10^{-5}	3.4	8.3×10^{-5}	4.5	2.4×10^{-4}	4.1	5.8×10^{-4}	4.4
	$\mathcal{G}^{(16)}$	1/160	4.8×10^{-6}	3.8	1.9×10^{-5}	4.4	5.8×10^{-5}	4.1	1.3×10^{-4}	4.3
rate			1.79		2.13		2.04		2.10	

Fig. 22. Vibrational modes of an annulus, case 2. Maximum errors and estimates convergence rates for traction boundary conditions at $t = 0.5$ with $\lambda/\mu = 1$.

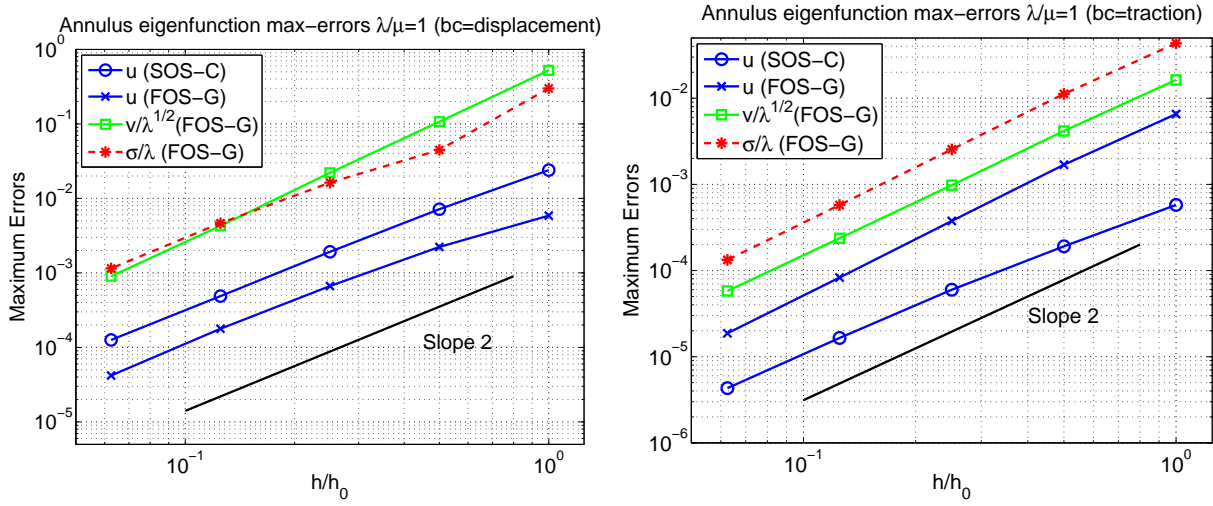


Fig. 23. Maximum errors in computing a time harmonic solution for an annulus at $t = 0.5$ with $\lambda/\mu = 1$. Left: case 1, displacement boundary conditions. Right: case 2, traction boundary conditions.

			SOS-C		FOS-G					
Grid	$\mathcal{G}^{(j)}$	$\Delta s^{(j)}$	$e_u^{(j)}$	r	$e_u^{(j)}$	r	$e_v^{(j)}$	r	$e_\sigma^{(j)}$	r
	$\mathcal{G}^{(1)}$	1/10	1.2×10^{-1}		2.5×10^{-1}		2.8×10^0		20.4×10^1	
	$\mathcal{G}^{(2)}$	1/20	4.1×10^{-2}	2.9	6.4×10^{-2}	3.9	1.3×10^0	2.2	51.5×10^0	4.0
	$\mathcal{G}^{(4)}$	1/40	1.2×10^{-2}	3.4	1.4×10^{-2}	4.6	4.0×10^{-1}	3.3	10.9×10^0	4.7
	$\mathcal{G}^{(8)}$	1/80	3.2×10^{-3}	3.7	2.9×10^{-3}	4.7	1.0×10^{-1}	3.8	2.3×10^0	4.8
	$\mathcal{G}^{(16)}$	1/160	8.2×10^{-4}	3.9	6.5×10^{-4}	4.5	2.6×10^{-2}	4.0	5.0×10^{-1}	4.6
rate			1.80		2.16		1.72		2.19	

Fig. 24. Vibrational modes of an annulus, case 3. Maximum errors and estimates convergence rates for displacement boundary conditions at $t = 0.5$ with $\lambda/\mu = 100$.

8.6. Vibrational modes of an elastic sphere

The vibration modes of an elastic sphere have been discussed, for example, by Lamb [25] and Love [24]. For verification we consider the following exact solution (a so-called solution of the *second class*) for a sphere of radius a ,

			SOS-C		FOS-G					
Grid	$\mathcal{G}^{(j)}$	$\Delta s^{(j)}$	$e_u^{(j)}$	r	$e_u^{(j)}$	r	$e_v^{(j)}$	r	$e_\sigma^{(j)}$	r
	$\mathcal{G}^{(1)}$	1/10	1.3×10^{-1}		1.7×10^{-1}		14.5×10^0		81.9×10^0	
	$\mathcal{G}^{(2)}$	1/20	4.6×10^{-2}	2.8	3.7×10^{-2}	4.5	2.9×10^0	5.0	18.7×10^0	4.4
	$\mathcal{G}^{(4)}$	1/40	1.3×10^{-2}	3.5	6.5×10^{-3}	5.8	5.2×10^{-1}	5.5	3.3×10^0	5.6
	$\mathcal{G}^{(8)}$	1/80	3.5×10^{-3}	3.8	9.9×10^{-4}	6.5	9.7×10^{-2}	5.4	5.2×10^{-1}	6.4
	$\mathcal{G}^{(16)}$	1/160	9.1×10^{-4}	3.9	1.5×10^{-4}	6.7	2.0×10^{-2}	4.9	7.9×10^{-2}	6.6
rate			1.81		2.55		2.40		2.52	

Fig. 25. Vibrational modes of an annulus, case 4. Maximum errors and estimates convergence rates for traction boundary conditions at $t = 0.5$ with $\lambda/\mu = 100$.

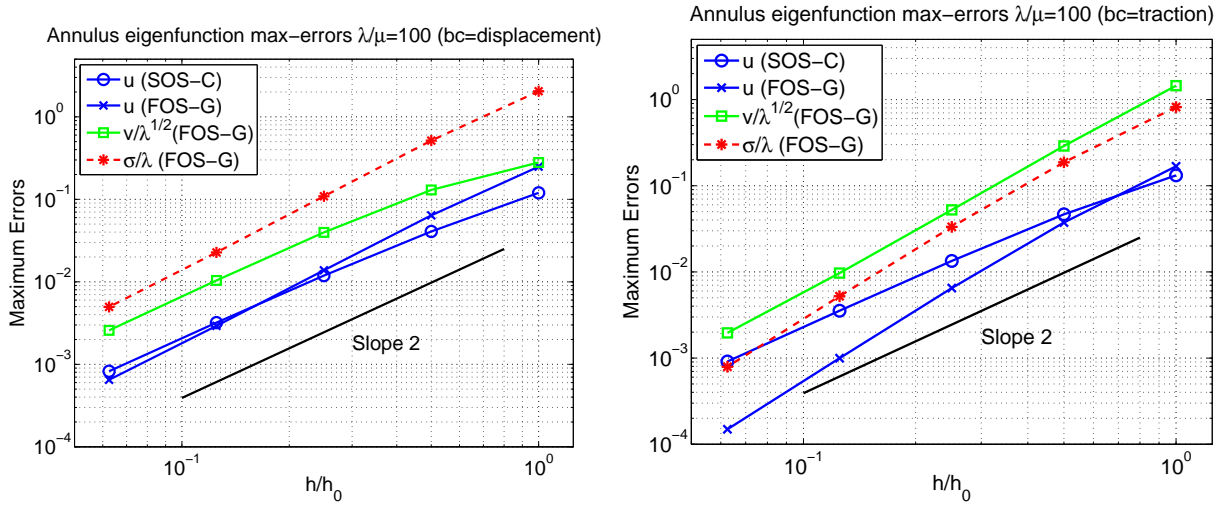


Fig. 26. $\lambda/\mu = 100$, maximum errors in computing a time harmonic solution for an annulus at $t = 0.5$ with $\lambda/\mu = 100$. Left: case 3, displacement boundary conditions. Right: case 4, traction boundary conditions. The errors for \mathbf{v} and $\boldsymbol{\sigma}$ are scaled to fit nicely on the graph.

$$\begin{aligned}
u_j^{(n)} = A \cos(\omega t) \Big\{ & -\frac{1}{\alpha^2} \left(\psi_n(\alpha r) \frac{\partial \zeta_n}{\partial x_j} + h^2 x_j \psi_{n+1}(\alpha r) \zeta_n \right) \\
& + \psi_{n-1}(\kappa r) \frac{\partial \chi_n}{\partial x_j} - \frac{n}{n+1} \kappa^2 \psi_{n+1}(\kappa r) \left(r^2 \frac{\partial \chi_n}{\partial x_j} - (2n+1) x_j \chi_n \right) \Big\}
\end{aligned} \quad (86)$$

where

$$\kappa^2 = \omega^2 \rho / \mu, \quad (87)$$

$$\alpha^2 = \omega^2 \rho / (\lambda + 2\mu), \quad (88)$$

$$\psi_n(x) = \left(\frac{1}{x} \frac{d}{dx} \right)^n \left(\frac{\sin(x)}{x} \right),$$

$$\chi_n(r, \theta, \phi) = C_{n,m} \zeta_n(r, \theta, \phi) = \mathcal{D}_{n,m} r^n e^{i\theta} P_n^l(\cos \phi), \quad (\text{solid spherical harmonic of order } n).$$

Here (r, θ, ϕ) are the spherical polar coordinates with radius r , $0 \leq r \leq a$, azimuthal angle θ , $0 \leq \theta \leq 2\pi$, and polar angle ϕ , $0 \leq \phi \leq \pi$. For each $n = 0, 1, 2, \dots$ there are an infinite number of eigenmodes, $m = 1, 2, \dots$, for particular values of $\omega = \omega_{n,m}$, $\kappa = \kappa_{n,m}$, and $\alpha = \alpha_{n,m}$. The eigenvalues are the roots of a certain *frequency* equation determined in the usual way by imposing the stress free boundary conditions on the surface of the sphere [24]. We consider, in particular, the mode $n = 2$ of the *spheroidal vibrations* in which case the solid spherical harmonic functions take the simple form

$$\zeta_2 = 2z^2 - x^2 - y^2,$$

$$\chi_2 = \mathcal{C}_{2,m}\zeta_2.$$

This solution corresponds to a mode where the sphere periodically becomes elongated and compressed along the z -axis as shown in Fig. 28. When the material satisfies Poisson's condition, $\lambda = \mu$, the first few eigenvalues are given in Fig. 27. Given values for $\kappa_{n,m}$, the values for $\omega_{n,m}$ and $\alpha_{n,m}$ are determined from (87) and (88).

m	$\kappa_{n,m} a/\pi$	$\mathcal{C}_{n,m}$
1	0.840296489389027	-0.375375159272393
2	1.54866444711667	-0.0798905931500425
3	2.65126525857435	0.0464019111586348

Fig. 27. First few roots of the frequency equation for spheroidal vibrations, $n = 2$ with $\lambda = \mu$. The spherical harmonics are related by $\chi_n = \mathcal{C}_{n,m}\zeta_n$.

An overlapping grid for the sphere, shown in Fig. 28, is defined by four component grids. A spherical shell defined with spherical polar coordinates is used as a body fitted grid over most of the sphere. The polar regions are covered with orthographic patches while a Cartesian grid occupies the interior of the sphere. To be more precise, define the spherical polar grid by

$$\mathcal{S}([\rho_a, \rho_b] \times [\theta_a, \theta_b] \times [\phi_a, \phi_b], N_1, N_2, N_3) = \{(\rho_{i_1} \cos \theta_{i_2} \sin \phi_{i_3}, \rho_{i_1} \sin \theta_{i_2} \sin \phi_{i_3}, \rho_{i_1} \cos \phi_{i_3}) \mid$$

$$\rho_{i_1} = \rho_a + i_1(\rho_b - \rho_a)/N_1, \theta_{i_2} = \theta_a + i_2(\theta_b - \theta_a)/N_2, \phi_{i_3} = \phi_a + i_3(\phi_b - \phi_a)/N_3,$$

$$i_\alpha = 0, 1, \dots, N_\alpha, \alpha = 1, 2, 3\}.$$

The cap grids are orthographic grids given by equation (79). The grid for the solid sphere, with resolution factor j , is composed of the box, sphere and two orthographic grids,

$$\mathcal{G}_{ss}^{(j)} = \mathcal{B}([-x_a, x_a]^3, N_x(j), N_x(j), N_x(j)) \cup \mathcal{S}([R_a, R_b] \times [0, 2\pi] \times [0, 2\pi], N_r(j), N_\theta(j), N_\phi(j))$$

$$\cup \mathcal{O}_{\pm 1}([R_a, R_b], S_a, S_a, N_r(j), N_0(j), N_0(j)),$$

where $h_j = 1/(10j)$, $R_a = .75$, $R_b = 1$, $x_a = R_a + 1.5h_j$, $N_x(j) = \lfloor 2x_a/h_j \rfloor$, $N_r(j) = \lfloor (R_b - R_a)/h_j + 1.5 \rfloor$, $N_\theta(j) = \lfloor 2\pi(.7R_b)/h_j + 1.5 \rfloor$, $N_\phi(j) = \lfloor (.6)(.85)\pi/h_j + 1.5 \rfloor$, $S_a = .65 + h_j$, and $N_0(j) = \lfloor (.7)S_a\pi(.7R_b)/h_j + 1.5 \rfloor$.

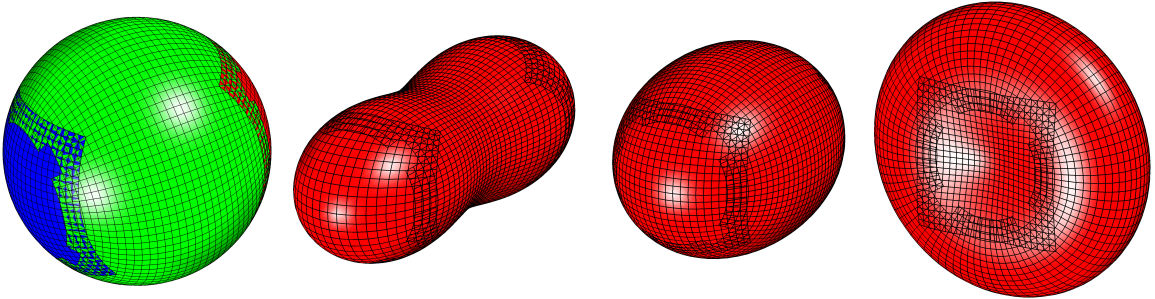


Fig. 28. Vibrational mode of an elastic sphere. Left: overlapping grid for a solid sphere consisting of two orthographic patches, a spherical polar shell and an interior Cartesian grid (not shown). Middle to right: the deformed sphere at times $t = 0$, $t = 0.8$ and $t = 1.2$, scaling the displacement by a factor of 0.08.

Fig. 29 shows the maximum errors and convergence rates for vibrational mode with $n = 2$ and $m = 1$. We choose the amplitude A in equation (86) as $A = 50/a$ so that the maximum displacements are about 1. From the figure we see that the solutions from the SOS-C and FOS-G schemes are converging at a rate close to 2.

			SOS-C		FOS-G					
Grid	$\mathcal{G}^{(j)}$	h_j	$e_u^{(j)}$	r	$e_u^{(j)}$	r	$e_v^{(j)}$	r	$e_\sigma^{(j)}$	r
	$\mathcal{G}_{ss}^{(1)}$	1/10	1.3×10^{-1}		5.1×10^{-2}		1.2×10^{-1}		2.6×10^{-1}	
	$\mathcal{G}_{ss}^{(2)}$	1/20	4.0×10^{-2}	3.2	1.2×10^{-2}	4.2	3.0×10^{-2}	4.0	5.1×10^{-2}	5.1
	$\mathcal{G}_{ss}^{(4)}$	1/40	10.0×10^{-3}	4.0	2.4×10^{-3}	5.1	7.1×10^{-3}	4.2	8.6×10^{-3}	6.0
	$\mathcal{G}_{ss}^{(8)}$	1/80	2.4×10^{-3}	4.1	5.2×10^{-4}	4.6	1.7×10^{-3}	4.1	2.0×10^{-3}	4.3
rate			1.93		2.22		2.03		2.37	

Fig. 29. Maximum errors and estimated convergence rates for computing a vibrational mode of a solid sphere.

8.7. Diffraction of a p-wave “shock” by a cylindrical cavity

To illustrate the use of adaptive mesh refinement we consider the diffraction of a p-wave “shock” by a cylindrical void. The initial conditions are taken from an exact traveling wave solution for a p-wave with a piecewise constant velocity profile given by

$$\mathbf{u}(\xi) = \begin{cases} -\xi v_0/c_p \boldsymbol{\kappa} & \text{for } \xi < 0, \\ 0 & \text{for } \xi > 0, \end{cases}, \quad \mathbf{v}(\xi) = \begin{cases} v_0 \boldsymbol{\kappa} & \text{for } \xi < 0, \\ 0 & \text{for } \xi > 0, \end{cases},$$

$$\xi = \boldsymbol{\kappa} \cdot (\mathbf{x} - \mathbf{x}_0) - c_p t, \quad c_p = \sqrt{(\lambda + 2\mu)/\rho_0},$$

where $\boldsymbol{\kappa}$ defines the direction of propagation of the wave and \mathbf{x}_0 defines its position at $t = 0$. For the computations presented we take $\boldsymbol{\kappa} = [1, 0]^T$, $v_0 = c_p$, $\mathbf{x}_0 = [-1.25, 0]^T$, $\lambda = 1$ and $\mu = 1$. The composite grid for this diffraction computation is defined from a background square and annular grid (see Section 8.2 for definitions of the square and annular grids)

$$\mathcal{G}_d^{(j)} = \mathcal{R}([-3, 3]^2, N_x(j), N_x(j)) \cup \mathcal{A}([R, R + 7\Delta s^{(j)}], N_\theta(j), N_r),$$

where $\Delta s^{(j)} = 1/(10j)$, $R = .5$, $N_x(j) = \lfloor 6/\Delta s^{(j)} + 1.5 \rfloor$, $N_\theta(j) = \lfloor 2\pi(R + 3.5\Delta s^{(j)})/\Delta s^{(j)} + 1.5 \rfloor$, and $N_r = 7$.

Figure 30 shows results from an AMR computation of a traveling p-wave diffracting around a cylindrical cavity computed with FOS-G. The boundary condition on the cylinder is zero traction. The boundary conditions on the top and bottom of the square are slip-walls. One refinement level of refinement factor 4 was used. The p-wave shock hits the circular void causing cylindrical p- and s-wave reflected waves.

Figure 31 compares the results at time $t = 1.6$ for four cases: coarse grid with FOS-G and no AMR, fine grid with FOS-G and no AMR, SOS-C with AMR and FOS-G with AMR. The results from the computations all generally agree with the finer grids providing a sharper representation of the discontinuous parts of the solution. The FOS-G results for the speed, $|\mathbf{v}|$, are not as noisy as the SOS-C results. Note, however, that the velocity is directly computed by FOS-G while for the SOS-C scheme it is computed in a post-processing step by a finite difference approximation in time, $\mathbf{v}_i^n = (\mathbf{u}_i^n - \mathbf{u}_i^{n-1})/\Delta t$.

8.8. Performance

In this section we present some computer timing results for the two approaches. Note that in two dimensions SOS-C has 2 dependent variables compared to FOS-G which has 6. In three-dimensions SOS-C has 3 variables compared to FOS-G which has 15. A moderate attempt was made to optimize each code although further work would help. The FOS-G approximation, for example, currently computes all the components of the stress tensor which results in extra work since the tensor is symmetric.

Fig. 32 gives CPU timings for the three-dimensional computation of a vibrational mode of a sphere described in Section 8.6. The overlapping grid for this case was $\mathcal{G}_{ss}^{(20)}$ with approximately 34 million grid points. The overlapping grid has four component grids with the majority of the grid points (32 million) belonging to the Cartesian grid. For this grid there were 1.1 million overlapping grid interpolation points.

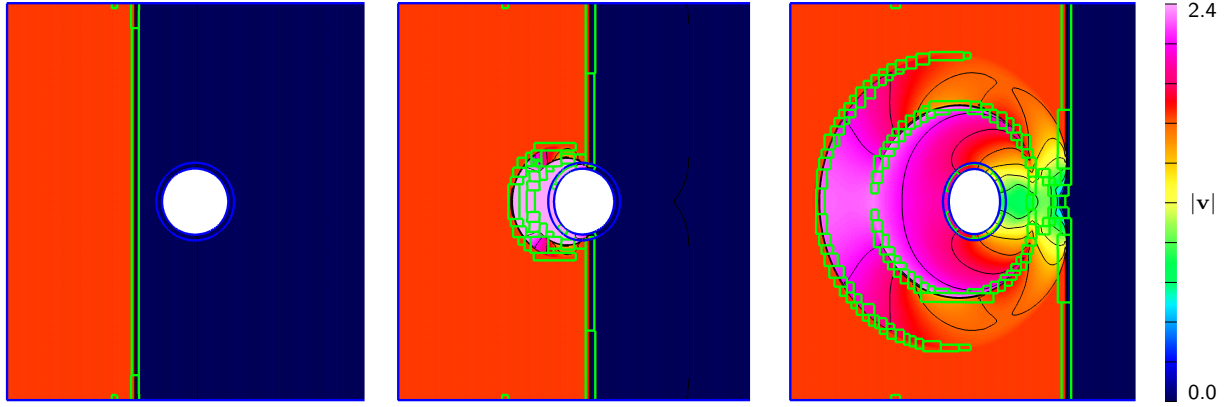


Fig. 30. Diffraction of a p-wave by a cylindrical cavity computed using AMR. Speed at times $t = 0$, $t = 0.8$ and $t = 1.6$ (FOS-G). The boundaries of the base overlapping grids are shown in blue and the boundaries of the refinement grids in green. The deformed grid is shown, scaling the displacement by a factor of 0.075.

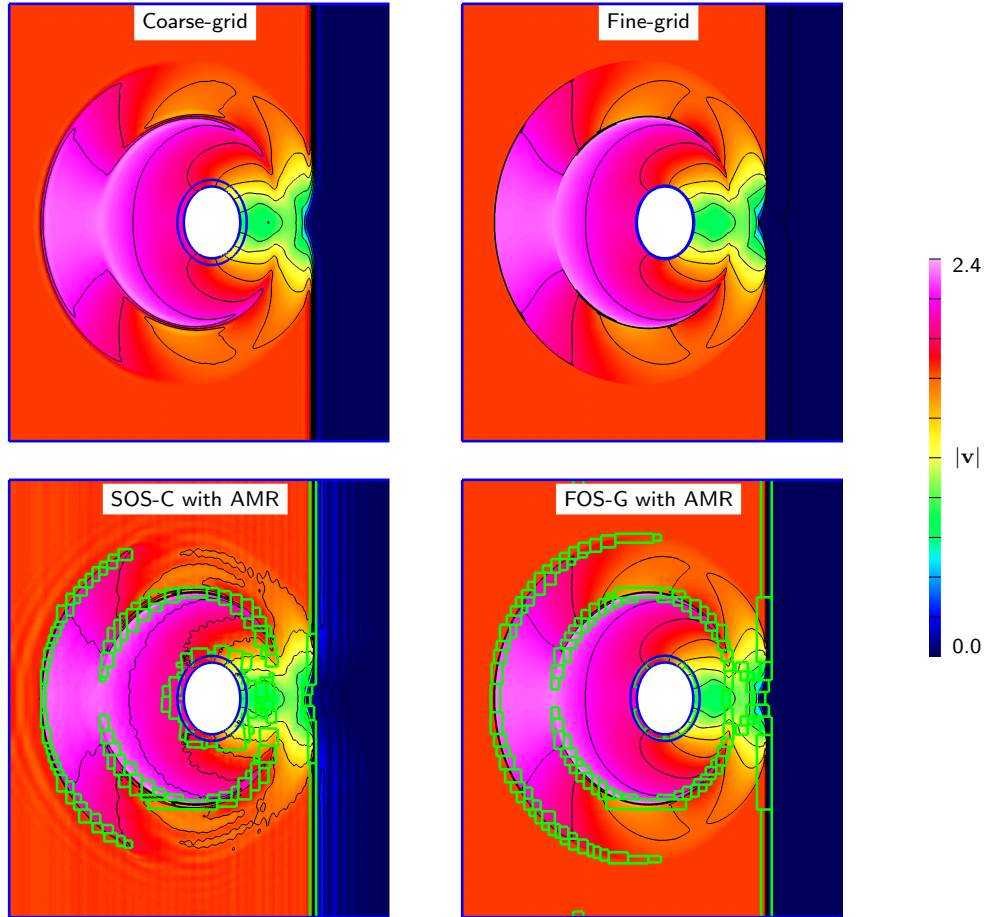


Fig. 31. Diffraction of a p-wave by a cylindrical cavity at time $t = 1.6$ computed with and without AMR. (a) coarse-grid, no-amr $\mathcal{G}^{(8)}$, (b) fine-grid, no-amr $\mathcal{G}^{(64)}$ (14.4M pts), (c) SOS-C with AMR $\mathcal{G}^{(8)}$, $l = 2$, $r = 4$, (d) FOS-G with AMR $\mathcal{G}^{(8)}$, $l = 2$, $r = 4$. The boundaries of the base grids are shown in blue and the boundaries of the refinement grids in green. The deformed grid is shown, scaling the displacement by a factor of 0.075.

Both codes have been optimized for the Cartesian grid case. The Cartesian grid discretization is significantly faster than the curvilinear approximation. (**number here ??**) The computation was run in parallel on 16

processors (4 nodes, 4 processors/node), using 2.4Ghz AMD Opteron processors with 16Gb per node. The times reported are the averaged values of the different processors. In the figure, the row label “advance” denotes the time spent advancing the interior equations (performed in the optimized Fortran routines) and does not include communication costs. The row labeled “interpolation” includes the cost for overlapping grid interpolation as well as updating the two layers of parallel ghost values.

From the SOS-C results one notes that the application of the sixth-order filter is relatively expensive (20% of the total time) compared to advancing the interior equations (45%). This is not surprising given that the filter is applied in two stages and requires a separate parallel ghost boundary update. In addition the majority of grid points are Cartesian where the discretization of the elasticity equations requires few operations. The interpolation and parallel ghost update is also relatively expensive at 20%. The parallel load balancer does not currently take the work required for interpolation into account and as a result the computation is not ideally balanced.

For the FOS-G scheme, approximately 67% of the time was spent advancing the interior equations. The FOS-G scheme, however, requires significantly more operations than the SOS-C scheme. Per time step, the FOS-G scheme was about $24.9/2.8 = 8.9$ times slower than the SOS-C scheme. In addition, the time-step for the FOS-G scheme was smaller than that for SOS-C by a factor of approximately $1/\sqrt{3} \approx 0.6$. This resulted in the SOS-C scheme being overall about 15.6 times faster than the FOS-G code. The SOS-C scheme used about one-third of the memory of the FOS-G scheme (0.6 Gb of memory per processor compared to 1.8 Gb).

Although more expensive in computational time and memory, we note that the FOS-G method generally provides more accurate results than the SOS-C scheme. The FOS-G solution on a coarse grid may be more accurate than the SOS-C scheme on a finer grid. Note that in three-dimensions the simulation time will roughly increase by a factor of 16 when the mesh spacing is decreased by a factor of 2. Thus even if the FOS-G scheme is 16 times slower (as with our current implementations), it still may be the better choice if it is more than 4 times more accurate.

Vibration of a Sphere (3D)						
	SOS-C			FOS-G		
	total (s)	s/step	%	total (s)	s/step	%
advance	90	1.3	45	2005	16.9	67.
boundary conditions	15	.22	7	51	.42	1.7
interpolation	41	.60	20	876	7.4	29.
filter	40	.58	20	0	0.	0.
other	5	.10	8	30	.18	2.3
total	190	2.8	100	2962	24.9	100

Fig. 32. CPU time (in seconds) for various parts of the code and their percentage of the total CPU time per step. Results for the vibrational modes of a sphere, grid $\mathcal{G}_{ss}^{(20)}$ with approximately 34 million grid points. The computation was run in parallel on 16 processors. The cost for parallel communication is included in the row labeled “interpolation”.

8.9. Three-dimensional circular plate with holes

As a final example, we consider an elastic disturbance propagating in a three-dimensional circular plate with holes, see Fig. 33. Without holes, the circular plate would occupy the domain $\Omega_p = \{(x, y, z) \mid x^2 + y^2 \leq R_p, 0 \leq z \leq W\}$ with outer radius $R_p = 4$ and thickness $W = 0.25$. Twenty-four small holes of radius 0.3 are located on equally spaced angles, $\theta_m = 15m^\circ$, $m = 0, 1, \dots, 23$ with centers on a radius of $r = 3.4$. Twelve larger holes of radius 0.4 are equally spaced on angles $\theta_m = (30m + 15)^\circ$, $m = 0, 1, \dots, 11$, centered on a radius of $r = 2.25$. Let $\mathcal{G}_p^{(j)}$ denote the overlapping grid for this domain where the grid spacing is approximately equal to $\Delta s^{(j)} = 1/(10j)$.

Traction boundary conditions (6) are given on all boundaries. The initial conditions are zero and define a plate at rest. A time-dependent traction forcing, $\mathbf{n} \cdot \boldsymbol{\tau} = \mathbf{g}_t$, is applied on the top surface at $z = W$. The forcing acts to first push down on the plate and then pull up and is defined by

$$\mathbf{g}_t(x, y, W, t) = -\hat{\mathbf{e}}_3 g(t) \exp(-20(x^2 + y^2)), \quad \hat{\mathbf{e}}_3 = [0, 0, 1]^T,$$

$$g(t) = \begin{cases} (p+1) 2^{2p+3} t^p (1-t)^p (\frac{1}{2} - t), & 0 \leq t \leq 1, \\ 0, & \text{otherwise,} \end{cases}$$

where p is chosen to be 3 so that the forcing turns smoothly on and off. Note that the integral of g from 0 to $\frac{1}{2}$ is 1 and the integral from 0 to 1 is zero. The material and elastic parameters are $\rho_0 = 1$, $\lambda = 1$ and $\mu = 1$.

Fig. 33 shows a coarsened version of the overlapping grid along with the evolution of the surface displacement. The disturbance is seen to propagate from the center of the plate outward. It diffracts and reflects first off the inner ring of larger holes and then the outer ring of smaller holes.

The solutions from the SOS-C and FOS-G schemes are compared in Fig. 35 at time $t = 3.0$ for the grid $\mathcal{G}_p^{(8)}$. Contours of the displacement norm, $|\mathbf{u}|$ are shown on the plane $z = W/2$. The results from the two schemes are nearly indistinguishable.

Given a sequence of three grids of increasing resolution, a posteriori estimates of the errors and convergence rates can be computed using the procedure described in [2]. These self-convergence estimates assume that the numerical results are converging to some limiting solution. The a posteriori estimates are given in Fig. 34 for grids $\mathcal{G}_p^{(j)}$ with $j = 4, 8, 16$. The finest grid, $\mathcal{G}_p^{(16)}$, has about 42 million active grid points. The estimated convergence rates for the maximum errors are close to the expected value of 2. The corresponding discrete L_2 -norm convergence rates are estimated to be 2.0 (to two significant figures) in all cases.

9. Conclusions

We have compared two approaches for solving the linear elastodynamic equations on overlapping grids. The SOS-C method solves the equations written as a second-order-system for the displacement using a second-order accurate conservative finite-difference approximation while the FOS-G scheme solves the first-order-system for the displacement, velocity and stress using a second-order accurate characteristic-based Godunov approach. Both methods were shown to be second-order accurate on a number of two- and three-dimensional test problems including a deforming annulus and deforming solid sphere where the exact solutions are known. A posteriori error estimates were determined for a complex example involving a three-dimensional circular plate with holes. In general the FOS-G approach provided more accurate results but was more expensive than the SOS-C scheme.

Our numerical scheme uses block-structured adaptive mesh refinement to dynamically add refinement grids where more accuracy is required. The AMR technique was illustrated in the computation of a p-wave “shock” hitting a cylindrical void.

An analysis of the scalar wave equation in second-order and first-order form on an overlapping grid showed that non-dissipative schemes (that are stable on a single grid) may have unstable modes on overlapping grids with growth rates proportional to the inverse of the mesh spacing. These unstable modes are generated by waves that become trapped in the region between an overlap and a nearby boundary. This instability also appears in the full elastic equations. A particularly difficult situation occurs with traction boundary conditions and the second-order-system when the ratio of λ/μ is large. In this case the SOS-C scheme can be effectively stabilized by the addition of an appropriate artificial dissipation or high-order filter. A sixth-order filter was shown to be a good choice. The upwinding properties of FOS-G, on the other hand, naturally stabilized the first-order-system scheme.

In future work we will consider material interfaces, variable material coefficients, high-order accurate methods and extensions of the equations to large deformations. The approach will also be used in the context of fluid-structure interaction problems.

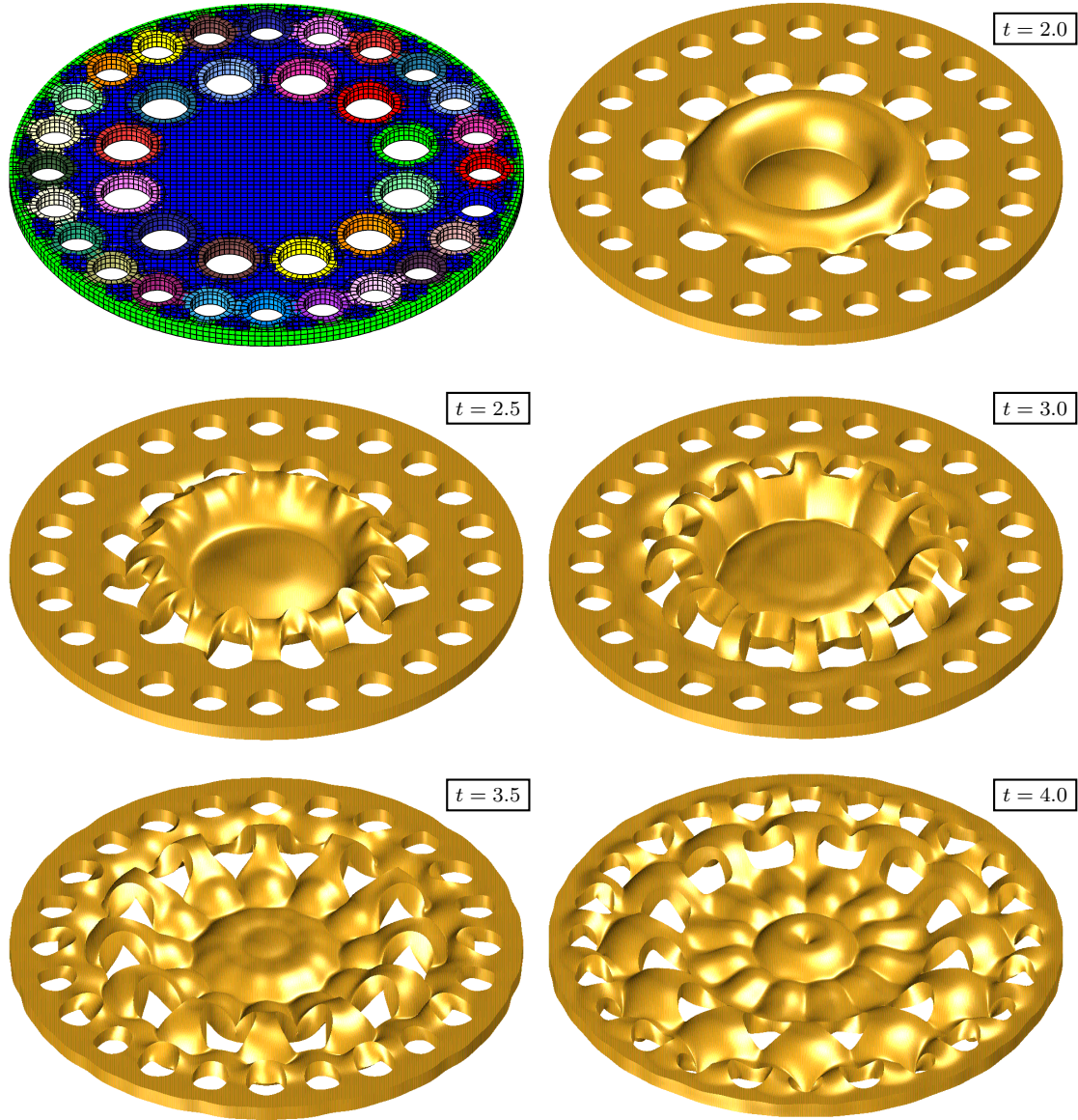


Fig. 33. Elastic waves in a three-dimensional circular plate with holes, composite grid (coarsened) and surface displacement at selected times. The deformed surface is shown with the displacement scaled by a factor of 3.

References

- [1] G. S. Chesshire, W. D. Henshaw, Composite overlapping meshes for the solution of partial differential equations, *J. Comput. Phys.* 90 (1) (1990) 1–64.
- [2] W. D. Henshaw, D. W. Schwendeman, Parallel computation of three-dimensional flows using overlapping grids with adaptive mesh refinement, *J. Comput. Phys.* 227 (16) (2008) 7469–7502.
- [3] W. M. Chan, Overset grid technology development at NASA Ames Research Center, *Computers and Fluids* 38 (3) (2009) 496–503.
- [4] W. D. Henshaw, A high-order accurate parallel solver for Maxwell’s equations on overlapping grids, *SIAM Journal on Scientific Computing* 28 (5) (2006) 1730–1765.
URL <http://link.aip.org/link/?SCE/28/1730/1>
- [5] R. J. Niethammer, K. S. Kim, J. Ballmann, Numerical simulation of shock waves in linear-elastic plates with curvilinear boundaries and material interfaces, *International Journal of Impact Engineering* 16 (1995) 1711–725.
- [6] X. Lin, J. Ballmann, A numerical scheme for axisymmetric elastic waves in solids, *Wave Motion* 21 (2) (1995) 115–126.

			SOS-C		FOS-G					
Grid	$\mathcal{G}^{(j)}$	h_j	$e_u^{(j)}$	r	$e_u^{(j)}$	r	$e_v^{(j)}$	r	$e_\sigma^{(j)}$	r
	$\mathcal{G}_p^{(4)}$	1/40	1.8×10^{-2}		9.5×10^{-3}		1.0×10^{-1}		1.3×10^{-1}	
	$\mathcal{G}_p^{(8)}$	1/80	4.5×10^{-3}	3.9	2.2×10^{-3}	4.2	2.8×10^{-2}	3.6	3.2×10^{-2}	3.9
	$\mathcal{G}_p^{(16)}$	1/160	1.2×10^{-3}	3.9	5.3×10^{-4}	4.2	7.7×10^{-3}	3.6	8.2×10^{-3}	3.9
rate			2.0		2.1		1.9		2.0	

Fig. 34. A posteriori estimated errors (max-norm) and convergence rates for computing elastic waves in a three-dimensional circular plate with holes at $t = 3.0$.

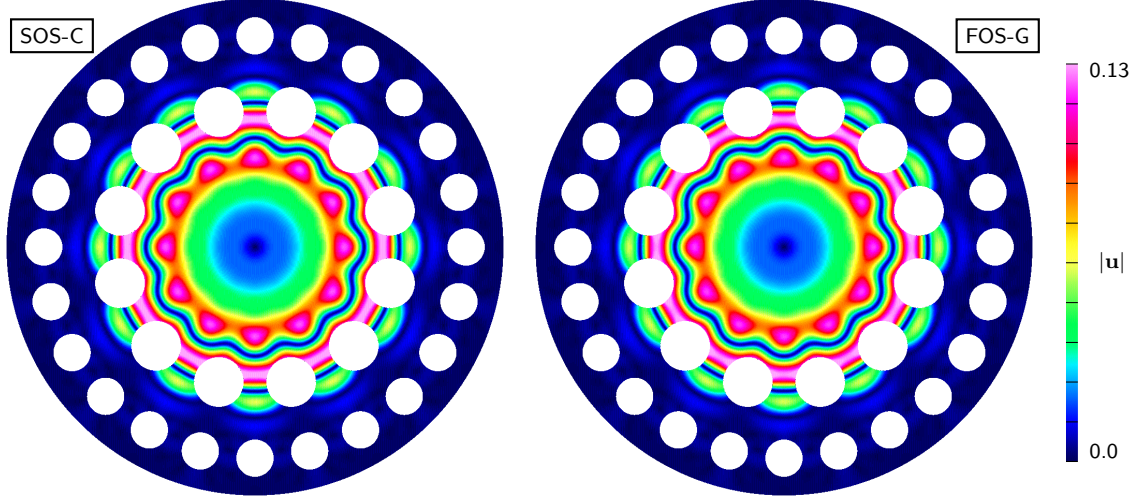


Fig. 35. Elastic waves in a three-dimensional circular plate with holes. Contours of the displacement, $|u|$, on the plane $z = 0.125$. Results for the grid $\mathcal{G}_p^{(8)}$ at $t = 3.0$ for SOS-C (left) and FOS-G (right).

- [7] D. Appelö, S. Nilsson, N. A. Petersson, B. Sjogreen, A stable finite difference method for the elastic wave equation on complex domains with free surface boundary conditions, Tech. Rep. UCRL_ABS-229550, Lawrence Livermore National Laboratory (2007).
- [8] W. D. Henshaw, Ogen: An overlapping grid generator for Overture, Research Report UCRL-MA-132237, Lawrence Livermore National Laboratory (1998).
- [9] D. Appelö, N. A. Petersson, A stable finite difference method for the elastic wave equation on complex geometries with free surfaces, Communications in Computational Physics 5 (2009) 84–107.
- [10] C. Bogey, C. Bailly, A family of low dispersive and low dissipative explicit schemes for flow and noise computations, J. Comput. Phys. 194 (1) (2004) 194–214.
- [11] S. K. Lele, Compact finite difference schemes with spectral-like resolution, Journal of Computational Physics 103 (1992) 16–42.
- [12] B. Gustafsson, H.-O. Kreiss, J. Oliger, Time Dependent Problems and Difference Methods, John Wiley and Sons Inc., 1995.
- [13] G. Browning, H.-O. Kreiss, J. Oliger, Mesh refinement, Mathematics of Computation 27 (121) (1973) 29–39.
- [14] M. Ciment, Stable difference schemes with uneven mesh spacings, Math. Comp. 25 (1971) 219–226.
- [15] M. J. Berger, Stability of interfaces with mesh refinement, Math. Comp. 45 (1985) 301–318.
- [16] G. Starius, On composite mesh difference methods for hyperbolic differential equations, Numer. Math. 35 (1980) 241–255.
- [17] L. G. M. Reyna, Part III. on composite meshes, Ph.D. thesis, Dept. of Applied Mathematics, California Institute of Technology (1982).
- [18] E. Pärt-Enander, B. Sjogreen, Conservative and non-conservative interpolation between overlapping grids for finite volume solutions of hyperbolic problems, Comput. Fluids 23 (3) (1994) 551–574.
- [19] F. Olsson, N. A. Petersson, Stability of interpolation on overlapping grids, Computers and Fluids 25 (1996) 583–605.
- [20] M. J. Berger, J. Oliger, Adaptive mesh refinement for hyperbolic partial differential equations, J. Comput. Phys. 53 (1984) 484–512.
- [21] M. J. Berger, P. Colella, Local adaptive mesh refinement for shock hydrodynamics, J. Comput. Phys. (1989) 64–84.
- [22] W. D. Henshaw, D. W. Schwendeman, An adaptive numerical scheme for high-speed reactive flow on overlapping grids, J. Comput. Phys. 191 (2003) 420–447.

- [23] P. J. Roache, Code verification by the method of manufactured solutions, ASME J. of Fluids Engineering 124 (1) (2002) 4–10.
- [24] A. E. H. Love, A Treatise on the Mathematical Theory of Elasticity, Dover Publications, New York, 1944.
- [25] H. Lamb, On the vibrations of an elastic sphere, Proceedings of the London Mathematical Society 13 (1882) 189–212.